J. Fluid Mech. (2014), *vol.* 749, *pp.* 597–626.
doi:10.1017/jfm.2014.209

Opposition control within the resolvent analysis framework

M. Luhar[1],†, A. S. Sharma[2] and B. J. McKeon[1]

[1]Graduate Aerospace Laboratories, California Institute of Technology, Pasadena, CA 91125, USA

[2]Engineering and the Environment, University of Southampton, Highfield, Southampton SO17 1BJ, UK

(Received 20 September 2013; revised 12 February 2014; accepted 12 April 2014;
first published online 19 May 2014)

This paper extends the resolvent analysis of McKeon & Sharma (*J. Fluid Mech.*, vol. 658, 2010, pp. 336–382) to consider flow control techniques that employ linear control laws, focusing on opposition control (Choi, Moin & Kim, *J. Fluid Mech.*, vol. 262, 1994, pp. 75–110) as an example. Under this formulation, the velocity field for turbulent pipe flow is decomposed into a series of highly amplified (rank-1) response modes, identified from a gain analysis of the Fourier-transformed Navier–Stokes equations. These rank-1 velocity responses represent propagating structures of given streamwise/spanwise wavelength and temporal frequency, whose wall-normal footprint depends on the phase speed of the mode. Opposition control, introduced via the boundary condition on wall-normal velocity, affects the amplification characteristics (and wall-normal structure) of these response modes; a decrease in gain indicates mode suppression, which leads to a decrease in the drag contribution from that mode. With basic assumptions, this rank-1 model reproduces trends observed in previous direct numerical simulation and large eddy simulation, without requiring high-performance computing facilities. Further, a wavenumber–frequency breakdown of control explains the deterioration of opposition control performance with increasing sensor elevation and Reynolds number. It is shown that slower-moving modes localized near the wall (i.e. attached modes) are suppressed by opposition control. Faster-moving detached modes, which are more energetic at higher Reynolds number and more likely to be detected by sensors far from the wall, are further amplified. These faster-moving modes require a phase lag between sensor and actuator velocity for suppression. Thus, the effectiveness of opposition control is determined by a trade-off between the modes detected by the sensor. However, it may be possible to develop control strategies optimized for individual modes. A brief exploration of such mode-optimized control suggests the potential for significant performance improvement.

Key words: drag reduction, turbulence control, turbulent boundary layers

† Email address for correspondence: mluhar@cantab.net

1. Introduction

Reducing turbulent skin friction on engineering surfaces (ships, aeroplanes, pipes, etc.) has the potential to yield tremendous environmental and economic benefits (Kim 2011; McKeon, Jacobi & Sharma 2013). As a result, considerable effort has been directed towards developing and evaluating control strategies for wall-bounded turbulent flows over the past three decades (Gad-el Hak 2000). This includes passive control involving two- or three-dimensional riblets and compliant surfaces (e.g. Bechert *et al.* 1997; Xu, Rempfer & Lumley 2003; Fukagata *et al.* 2008; Choi *et al.* 2012), open-loop active control (transverse wall oscillations, upstream-travelling waves of blowing and suction, streamwise waves of spanwise velocity at the wall (see e.g. Quadrio & Ricco 2004; Min *et al.* 2006; Quadrio, Ricco & Viotti 2009; Moarref & Jovanovic 2012)), as well as feedback flow control.

The area of feedback flow control has been especially active in recent years, with simulation and modelling efforts suggesting significant scope for drag reduction (e.g. Choi, Moin & Kim 1994; Koumoutsakos 1999; Lim & Kim 2004; Sharma *et al.* 2011). Of course, there are many challenges associated with making feedback flow control feasible, chief amongst which is the development of an effective and robust control law. Further, given the technical difficulties inherent in developing small reliable sensors and actuators (Cattafesta & Sheplak 2011), it must rely on quantities that can be measured easily in turbulent flows, and require actuation that is practicable.

1.1. *Feedback flow control*

Early studies in the realm of feedback flow control relied on physical insight to devise control laws. For example, the opposition control method of Choi *et al.* (1994) was developed to suppress the sweeps and ejections associated with the energetic coherent structures active in the near-wall region (Robinson 1991). Recognizing that opposition requires measurements inside the flow domain, Koumoutsakos (1999) proposed control on vorticity flux, which only requires wall-based sensing. Such physically motivated approaches have been broadly successful, with direct numerical simulation (DNS) showing drag reductions as large as 25 % and 40 % for opposition control and vorticity flux control, respectively. However, the reliance on expensive DNS for evaluation limits such studies to relatively low Reynolds numbers, and precludes a significant exploration of parameter space.

Recent advances in our understanding of wall turbulence have enabled significant further progress towards the design of effective control. Of particular importance has been the recognition that linear mechanisms play a key role in controlling the transition to turbulence at low Reynolds number (Trefethen *et al.* 1993; Henningson & Reddy 1994), as well as generating and sustaining the dynamically important coherent structures that characterize wall turbulence (e.g. Butler & Farrell 1993; Schoppa & Hussain 2002; Kim 2011). As a result, the application of concepts from control theory has led to the design of many successful control strategies that delay the onset of turbulence (Joshi, Speyer & Kim 1997), relaminarize turbulent flows (Högberg, Bewley & Henningson 2003; Sharma *et al.* 2011), or reduce turbulent kinetic energy (Lim & Kim 2004). Unfortunately, while such theoretical approaches lead to effective control laws, they can sometimes be difficult to interpret physically. The physically motivated studies described above provide insight into the mechanism of drag reduction, but they do not always lead to the best control strategy.

In an effort to bridge the physically motivated and theoretical approaches to flow control, this paper extends the resolvent analysis framework proposed by McKeon &

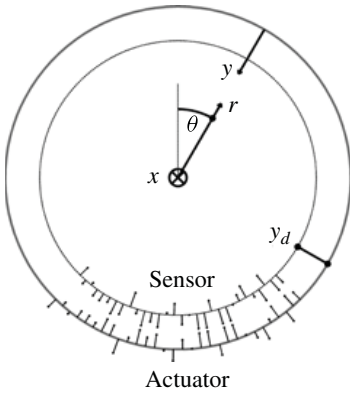

FIGURE 1. Schematic showing the coordinate system employed in this paper. The lower half of the schematic depicts opposition control. The wall-normal velocity is detected by a sensor at y_d. Blowing and suction are generated at the wall to oppose the detected velocity.

Sharma (2010). Recent studies show that simple rank-1 models based on the resolvent analysis capture many of the key statistical and structural features of wall turbulence (Moarref *et al.* 2013; Sharma & McKeon 2013). In addition to being computationally cheap and physically insightful, this approach is also amenable to the application of rigorous control theory. This paper focuses on the opposition control method proposed by Choi *et al.* (1994). However, the approach described herein can be extended to any control technique that employs a linear control law.

1.2. *Previous results for opposition control*

As one of the earliest proposed feedback flow control methods, opposition control (Choi *et al.* 1994) often serves as a benchmark against which newer methods are evaluated. Under opposition control, the wall-normal velocity, v, is measured at a specified detection plane, y_d, and blowing and suction are applied at the wall ($y = 0$) that is equal and opposite to the measured velocity (figure 1). Physically, the goal of this method is (i) to sense the sweeps and ejections associated with the dynamically important coherent structures active in the near-wall region, and (ii) to suppress them by opposing their motion.

DNS studies (Choi *et al.* 1994; Chung & Talha 2011) show that opposition control yields skin friction reductions as large as 25 % at low Reynolds number in channel flows ($Re_\tau = u_\tau h/\nu = 180$, based on channel half-height h, friction velocity u_τ and kinematic viscosity ν). However, control performance is strongly dependent on the location of the detection plane. Maximum drag reduction is achieved with the detector at $y_d^+ \approx 15$, and drag increases substantially for $y_d^+ > 25$ (Chung & Talha 2011). Fukagata & Kasagi (2002) studied the effectiveness of opposition control in turbulent pipe flow at $R^+ = 180$ (where R is the pipe radius, and superscript $+$ denotes normalization with respect to the inner units, u_τ and ν) and obtained similar results.

For cases where opposition control is effective and drag is reduced, DNS observations show that a virtual wall (i.e. near-zero wall-normal velocity fluctuations) is established at a location between the detection plane and the wall (Hammond, Bewley & Moin 1998). This virtual wall hinders the transfer of momentum in the wall-normal direction, which leads to a reduction in near-wall turbulence intensities. Yet, the deterioration in performance with increasing detection plane elevation is

not fully understood. Further, large eddy simulation (LES) studies have shown that opposition control does not scale well with Reynolds number. The maximum drag reduction reduces to 17.9 % for $Re_\tau = 960$ (Pamies *et al.* 2007). These Reynolds-number trends also remain to be explained.

1.3. *Approach and outline*

As noted earlier, this paper develops a simple model for opposition control based on the resolvent analysis proposed by McKeon & Sharma (2010). This analysis identifies the Fourier-transformed Navier–Stokes equations as a linear input–output system (see § 2.1). The nonlinear convective terms are treated as a forcing (input) to the system, and the turbulent velocity field is the response (output). At each wavenumber–frequency combination, the Navier–Stokes resolvent operator is the transfer function that maps the nonlinear forcing to a velocity response. A gain analysis (singular value decomposition) of the resolvent operator identifies the forcing that leads to the largest velocity response, and this large (rank-1) velocity response is assumed to dominate the flow field at that wavenumber–frequency combination. The effect of opposition control is introduced in this framework via the boundary condition on wall-normal velocity. The effectiveness of control is determined by the change in the amplification characteristics and structure of the rank-1 velocity responses. A decrease in amplification is interpreted as mode suppression, which leads to drag reduction (§ 2.3).

There are conceptual similarities between the model developed here, and the singular value analysis of boundary layer control pursued by Lim & Kim (2004). Using a singular value decomposition, Lim & Kim (2004) estimated the transient growth of optimal initial disturbances (i.e. disturbances with the largest growth ratio) to the linearized Navier–Stokes system. The effectiveness of control was determined by the change in the growth ratio (singular values) under control, whereby a decrease in the growth ratio was interpreted as a decrease in the turbulence intensity. However, there are two key differences between the model developed here and the analysis of Lim & Kim (2004). First, instead of considering the growth of optimal initial disturbances to the linearized Navier–Stokes system, this paper considers the flow response to continuous forcing from the nonlinear convective terms. Second, the velocity responses obtained under the present analysis at each wavenumber–frequency combination represent distinct flow structures (Sharma & McKeon 2013), and so the model developed here permits greater physical interpretation. We note that Brandt *et al.* (2011) have employed a similar formulation to study the effect of modifications to the laminar base flow on noise amplification in flat-plate boundary layers.

The remainder of this paper is structured as follows. Section 2.1 provides a brief review of the resolvent analysis, and § 2.2 describes the velocity structure typical of rank-1 resolvent modes. Section 2.3 describes the implementation of opposition control within the resolvent analysis framework, and develops a simple rank-1 model that is used to predict drag reduction. One of the advantages of the approach developed here is that it allows the effects of control to be studied on a mode-by-mode basis. As a result, this paper first considers the effect of opposition control on the structure and amplification of individual response modes (§§ 3.1 and 3.2). Model predictions for the effect of control in spectral space and drag reduction are presented next, in §§ 3.3 and 3.4, respectively. The potential for improved performance through amplitude- and phase-optimized wall blowing and suction is explored in §§ 3.5 and 3.6.

Two different Reynolds numbers are considered in this paper: $Re = 2\bar{U}R/\nu = 5300$ ($R^+ = 180$) and $Re = 44\,000$ ($R^+ = 1100$), where R is the pipe radius and $\bar{U}$ is the

bulk-averaged velocity. These Reynolds numbers correspond roughly to the lowest and highest limits at which existing results for opposition control are available. However, unlike DNS and LES, the model developed here is not limited to low Reynolds number due to computational expense. Beyond the requirement of a mean velocity profile in the resolvent operator (§ 2.1), higher Reynolds numbers do not pose a significant challenge. Indeed, all of the results presented in this paper were obtained on a laptop computer.

2. Approach

This section provides a brief review of the resolvent analysis of McKeon & Sharma (2010), before presenting a rank-1 model for opposition control. Note that a rank-1 assumption is made here for simplicity. The introduction of further complexity (i.e. a higher-rank approximation) is possible. Further, this paper only considers fully developed turbulent pipe flow to maintain consistency with the work of McKeon & Sharma (2010), who chose the cylindrical geometry for the integer constraint it poses on azimuthal wavenumber and due to the availability of experimental mean velocity profiles to truly high Reynolds number for turbulent pipe flow (McKeon *et al.* 2004). However, given the similarity in near-wall flow characteristics (Monty *et al.* 2009) and opposition control efficacy (Fukagata & Kasagi 2002) observed across geometries, the results are expected to be generally applicable.

2.1. *Resolvent analysis*

Given the cylindrical geometry, the statistical homogeneity in the streamwise (x) direction and stationarity in time (t), the total velocity field $\tilde{\boldsymbol{u}}$ for fully developed turbulent pipe flow can be expressed as a superposition of Fourier modes with streamwise wavenumber k, spanwise wavenumber n (constrained to be an integer) and temporal frequency ω:

$$\tilde{\boldsymbol{u}}(x, y, \theta, t) = \sum_n \int_{-\infty}^{\infty} \int_{-\infty}^{\infty} \boldsymbol{u}_{\boldsymbol{k}}(y) \mathrm{e}^{\mathrm{i}(kx+n\theta-\omega t)} \,\mathrm{d}k \,\mathrm{d}\omega. \tag{2.1}$$

Each wavenumber–frequency combination, $\boldsymbol{k} = (k, n, \omega)$, represents a helical wave propagating downstream with speed $c = \omega/k$. The turbulent mean velocity profile is $\boldsymbol{u_0} = (U(y), 0, 0)$, and so the fluctuating velocity field is $\boldsymbol{u} = (u, v, w) = \tilde{\boldsymbol{u}} - \boldsymbol{u_0}$. Here, the first ($U$, u), second (v) and third (w) components of the velocity field represent the streamwise, wall-normal and azimuthal velocities, respectively.

With this Fourier decomposition, at each $\boldsymbol{k}$ the Navier–Stokes equations for turbulent pipe flow can be expressed in dimensionless form as

$$(-\mathrm{i}\omega + \mathrm{i}kU)\boldsymbol{u}_{\boldsymbol{k}} + v_k U' \boldsymbol{e_x} + \boldsymbol{\nabla} p_k - Re^{-1}\nabla^2 \boldsymbol{u}_{\boldsymbol{k}} = \boldsymbol{f}_{\boldsymbol{k}}, \tag{2.2}$$

$$\boldsymbol{\nabla} \cdot \boldsymbol{u}_{\boldsymbol{k}} = 0. \tag{2.3}$$

Here, p_k is the Fourier-transformed fluctuating pressure field, U' is the mean shear and $\boldsymbol{f}_{\boldsymbol{k}} = (-\boldsymbol{u} \cdot \boldsymbol{\nabla}\boldsymbol{u})_{\boldsymbol{k}}$ represents the nonlinear convective terms. Note that $\boldsymbol{u}_{\boldsymbol{k}}$, p_k and $\boldsymbol{f}_{\boldsymbol{k}}$ are complex Fourier coefficients that vary in the wall-normal, or radial, direction. Rearranging (2.2) and (2.3) yields the following input–output (or forcing–response) relationship:

$$\begin{aligned} \begin{bmatrix} \boldsymbol{u}_{\boldsymbol{k}} \\ p_k \end{bmatrix} &= \left(-\mathrm{i}\omega \begin{bmatrix} \boldsymbol{I} & \\ & 0 \end{bmatrix} - \begin{bmatrix} \boldsymbol{\mathcal{L}}_{\boldsymbol{k}} & -\boldsymbol{\nabla} \\ \boldsymbol{\nabla}^{\mathrm{T}} & 0 \end{bmatrix} \right)^{-1} \begin{bmatrix} \boldsymbol{I} & \\ & 0 \end{bmatrix} \boldsymbol{f}_{\boldsymbol{k}} \\ &= \boldsymbol{\mathcal{H}}_{\boldsymbol{k}} \boldsymbol{f}_{\boldsymbol{k}}. \end{aligned} \tag{2.4}$$

The nonlinear terms, $\boldsymbol{f}_k$, are identified as a forcing to the linear Navier–Stokes system. The resolvent operator, $\boldsymbol{\mathcal{H}}_k$, maps this forcing to a velocity response, $\boldsymbol{u}_k$. The first row inside the parentheses on the right-hand side of (2.4) represents the momentum equations, while the last row represents continuity. Here $\boldsymbol{\mathcal{L}}_k(\boldsymbol{k}, U, Re)$ is the linear Navier–Stokes operator:

$$\boldsymbol{\mathcal{L}}_k = \begin{bmatrix} -\mathrm{i}kU + \dfrac{D + r^{-2}}{Re} & -\dfrac{\partial U}{\partial r} & 0 \\ 0 & -\mathrm{i}kU + \dfrac{D}{Re} & -\dfrac{2\mathrm{i}nr^{-2}}{Re} \\ 0 & +\dfrac{2\mathrm{i}nr^{-2}}{Re} & -\mathrm{i}kU + \dfrac{D}{Re} \end{bmatrix}, \tag{2.5}$$

where $D = -k^2 - (n^2 + 1)r^{-2} + \partial_r^2 + r^{-1}\partial_r$ represents the Laplacian. Note that this paper employs both radial and wall-normal coordinates. For notational convenience, most mathematical operations are presented in terms of the radial coordinate (r) and velocity ($\hat{v}_k$). The results are presented exclusively in terms of the wall-normal coordinate (y) and velocity (v_k), to ensure consistency with boundary layer and channel flow studies.

Following McKeon & Sharma (2010), a singular value decomposition of the resolvent operator, $\boldsymbol{\mathcal{H}}_k$, discretized using a Chebyshev collocation method, identifies an ordered set of orthonormal forcing and response modes for each wavenumber–frequency combination:

$$\boldsymbol{\mathcal{H}}_k = \sum_m \boldsymbol{u}_{k,m}\sigma_{k,m}\boldsymbol{f}^*_{k,m} \tag{2.6}$$

with

$$\sigma_{k,1} > \sigma_{k,2} > \cdots > \sigma_{k,m} > 0, \tag{2.7}$$

$$\int_0^1 \boldsymbol{f}^*_{k,l}\boldsymbol{f}_{k,m} r\,\mathrm{d}r = \delta_{lm}, \qquad \int_0^1 \boldsymbol{u}^*_{k,l}\boldsymbol{u}_{k,m} r\,\mathrm{d}r = \delta_{lm}. \tag{2.8a,b}$$

Here, the asterisk denotes the complex conjugate. From (2.4)–(2.8), it can be seen that the forcing mode $\boldsymbol{f}_{k,1}$ leads to the most amplified (highest σ_k) velocity response $\boldsymbol{u}_{k,1}$, based on an L^2 (energy) norm. Drawing a rough analogy to linear stability theory, the response mode $\boldsymbol{u}_{k,1}$ may be interpreted as the least damped velocity field for the wavenumber combination $\boldsymbol{k} = (k, n, \omega)$. This velocity field is sustained by minimal forcing of the form $\boldsymbol{f}_{k,1}$. The magnitude of the forcing required for a response of unit amplitude decreases with increasing $\sigma_{k,1}$. Conversely, for unit forcing across all modes, velocity responses with the highest amplification (highest σ_k) dominate the flow field.

Following Meseguer & Trefethen (2003), McKeon & Sharma (2010) projected the Navier–Stokes equations onto divergence-free basis functions that satisfied the correct boundary conditions ($\boldsymbol{u}_k = 0$ at the wall). This projection satisfies mass continuity and eliminates the pressure gradient term, such that the resolvent operator in (2.4) becomes $\boldsymbol{\mathcal{H}}_k = (-\mathrm{i}\omega\boldsymbol{I} - \boldsymbol{\mathcal{L}}_k)^{-1}$. However, to account for the effects of wall-based actuation due to opposition control, this projection is not employed here. Pressure and mass continuity are retained explicitly, and so a singular value decomposition of $\boldsymbol{\mathcal{H}}_k$ identifies the most amplified divergence-free velocity response, $\boldsymbol{u}_k$, as well as the associated pressure field, p_k (Luhar, Sharma & McKeon 2013). Despite this difference in formulation, the velocity response modes and singular values identified here are

almost identical to those obtained by McKeon & Sharma (2010). For all the mode combinations considered by McKeon & Sharma (2010), the singular values obtained with the present formulation converge to within 1 % of those obtained by McKeon & Sharma (2010) and the velocity response magnitudes agree within 0.01 for grid resolutions $N > 150$ for $r \in (0, 1]$.

Given the form of the resolvent operator in (2.4), McKeon & Sharma (2010) suggest that large amplification (high $\sigma_{\boldsymbol{k}}$) can arise via two mechanisms: (i) through the linear coupling between mean shear (U') and wall-normal velocity ($v_{\boldsymbol{k}}$), which is responsible for the non-normal nature of the resolvent operator; and (ii) when the velocity responses are localized near a critical layer y_c, where the phase speed of the modes matches the local mean velocity $c = \omega/k = U(y_c)$, such that the diagonal term $(kU - \omega) \approx 0$. Although both mechanisms responsible for high amplification are linear, the nonlinearity still plays a role: there must be some forcing present in the flow for the high amplification to be translated into a large velocity response.

Importantly, analysis of the resolvent operator for $\boldsymbol{k}$ combinations prevalent in natural turbulence suggests a low-rank system (Moarref *et al.* 2013); the first singular values tend to be much larger than the rest, $\sigma_{\boldsymbol{k},1} \gg \sigma_{\boldsymbol{k},2}$. So, the first singular response mode $\boldsymbol{u}_{\boldsymbol{k},1}$ is expected to dominate the velocity field, as long as some forcing exists in the direction of $\boldsymbol{f}_{\boldsymbol{k},1}$ in the real flow. Indeed, recent studies (Moarref *et al.* 2013; Sharma & McKeon 2013) have shown that rank-1 models ($\boldsymbol{u}_{\boldsymbol{k}} \sim \boldsymbol{u}_{\boldsymbol{k},1}$) capture many key statistical and structural features of wall turbulence. As a result, only the first singular response modes are retained for the remainder of this paper, and the additional subscript 1 is dropped for convenience.

Finally, note that the analysis presented in (2.4)–(2.8) does not represent a linearization of the Navier–Stokes equations. The system of equations shown in (2.4) is exact if the full nonlinear velocity field is available. However, in the absence of such information, the gain-based decomposition shown in (2.6)–(2.8), coupled with simple assumptions regarding the nonlinear forcing, can provide significant insight into the turbulent flow field. Of course, this decomposition does assume that the nonlinearity has already acted to support the base flow, i.e. the assumed mean velocity profile, U, in $\boldsymbol{\mathcal{H}}_{\boldsymbol{k}}$ (2.4).

2.2. *Structure of rank-1 response modes*

As an example, figure 2 shows the rank-1 velocity response obtained under the resolvent analysis for the wavenumber–frequency combination $\boldsymbol{k} = (k, n, c = \omega/k) = (6, \pm 60, 0.45)$ at $R^+ = 1100$. This mode represents helical waves of streamwise wavelength $\lambda_x^+ = 2\pi R^+/k \approx 1200$ and azimuthal wavelength $\lambda_\theta^+ = 2\pi R^+/n \approx 120$, propagating downstream at 45 % of the pipe centreline velocity $c^+ = 0.45 U_{CL}^+ \approx 11$. Note that $n = +60$ represents a right-handed helical wave while $n = -60$ represents a left-handed helical wave. Aside from this chirality, right- and left-handed modes are structurally similar. The velocity structure shown in figure 2 includes contributions from both $+n$ and $-n$. Velocity isosurfaces for either the $+n$ or $-n$ modes align obliquely to the x axis. With contributions from both the $+n$ and $-n$ modes, the velocity structure aligns with the x axis (figure 2*a*). As expected for Fourier modes, the isosurfaces of streamwise velocity show alternating regions of positive and negative velocity with streamwise and spanwise wavelengths set by k and n. The wave speed c can be thought of as the convection velocity for the velocity structure associated with this mode combination.

Figure 2 shows that the location of the maximum streamwise velocity coincides roughly with the location of the critical layer for this mode ($y_c^+ = 16$), where the mean

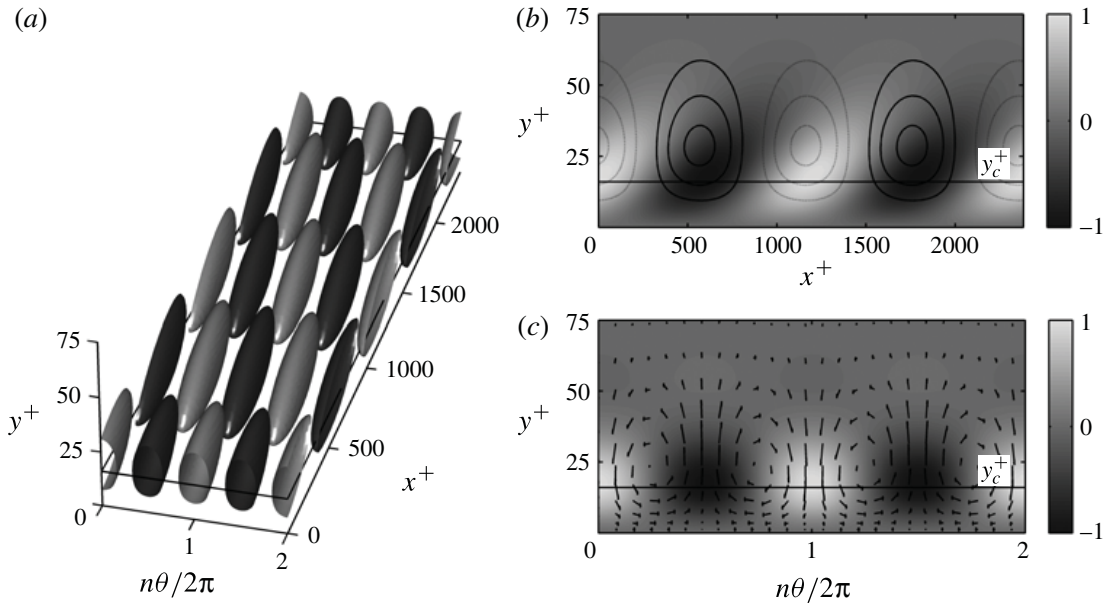

FIGURE 2. (*a*) Isosurfaces of streamwise velocity (at 50 % of maximum) for the combination of left- and right-helical modes $\boldsymbol{k} = (6, \pm 60, 0.45)$ at $R^+ = 1100$. Light shading denotes positive u and dark shading denotes negative u. (*b*) Velocity isocontours in the streamwise–wall normal plane corresponding to $n\theta = 0$. The shading represents the streamwise velocity distribution. The solid and dashed lines represent positive and negative wall-normal velocity, respectively (at $\pm 0.3,\ 0.6,\ 0.9$ of maximum). (*c*) Velocity structure in the azimuthal–wall normal plane corresponding to $x^+ = 0$. The shading represents the streamwise velocity while the arrows denote the wall-normal and azimuthal velocity fields (not to scale). The critical layer for the mode falls at $y_c^+ = 16$ (solid horizontal line). Note that the velocity structure shown in this figure is for the uncontrolled resolvent modes.

velocity matches the wave speed $U^+(y_c^+) = c^+$. The wall-normal velocity is maximum at a location slightly further away from the wall ($y^+ \approx 30$, figures 2*b* and 3*a*). The streamwise velocity isocontours exhibit a slight inclination in the streamwise–wall normal plane, but the wall-normal velocity isocontours remain vertical (figure 2*b*). Near the critical layer, regions of positive wall-normal velocity coincide with regions of negative streamwise velocity. In the spanwise–wall normal plane, the velocity structure associated with this mode clearly shows the existence of counter-rotating quasi-streamwise vortices (figure 2*c*). Consistent with the isocontours in figure 2(*b*), the wall-normal velocity associated with these streamwise vortices is negative in regions of positive $u_{\boldsymbol{k}}$ (at $n\theta/2\pi = 1$) and positive in regions of negative $u_{\boldsymbol{k}}$ (at $n\theta/2\pi = 0.5$ and 1.5).

Localization of the streamwise velocity around y_c^+ indicates that the critical-layer mechanism plays a role for this mode. In addition, the velocity structure shown in figure 2(*c*) suggests that the non-normal interaction between the mean shear U' and wall-normal velocity $v_{\boldsymbol{k}}$ is also important. For positive $v_{\boldsymbol{k}}$, this interaction transfers fluid with low streamwise momentum away from the wall. For negative $v_{\boldsymbol{k}}$, high-momentum fluid is brought towards the wall. Thus, regions of positive $v_{\boldsymbol{k}}$ coincide with regions of negative $u_{\boldsymbol{k}}$, and vice versa. Indeed, if the mean shear U' is artificially set to zero in the discretized resolvent operator, this interaction (also referred to as lift-up) is eliminated and the singular value for this response mode drops by an order of magnitude, from $\sigma_{\boldsymbol{k}0} = 29.5$ to $\sigma_{\boldsymbol{k}0} = 3.0$.

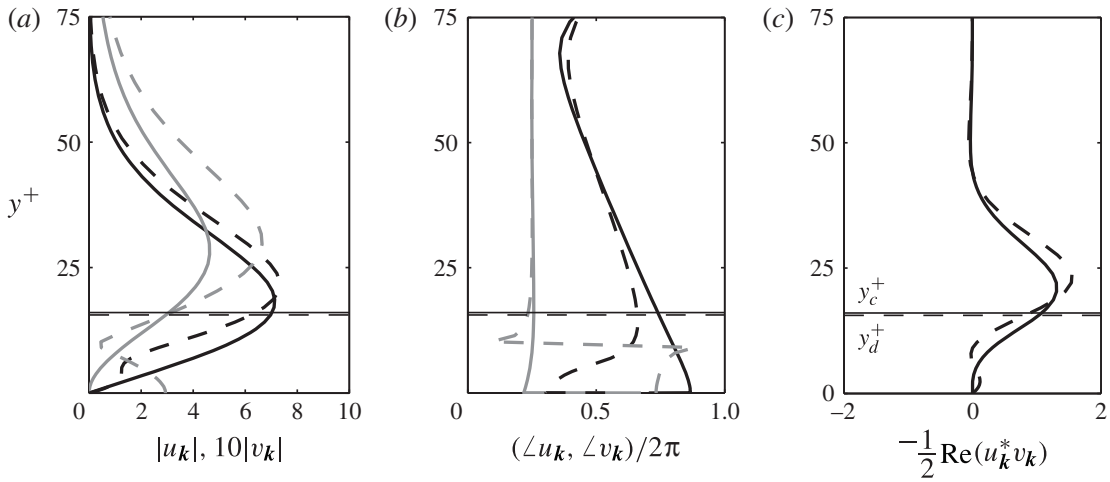

FIGURE 3. Vertical profiles showing (*a*) the amplitude and (*b*) the phase of the streamwise (black) and wall-normal (grey) velocity for mode $\boldsymbol{k} = (k, n, c) = (6, 60, 0.45)$ at $R^+ = 1100$. (*c*) The Reynolds stress contribution from this mode. Solid lines show the null case, and dashed lines represent the controlled case with the detector at $y_d^+ \approx 15$. Horizontal lines show the critical layer ($y_c^+ = 16$) and the true detection plane ($y_d^+ = 15.6$). The singular values for this mode decrease under control, from $\sigma_{k0} = 29.5$ to $\sigma_{kc} = 18.1$.

Many of the structural features shown in figure 2 are typical of the velocity response modes obtained under the resolvent analysis. Contours of u_k tend to be inclined in the streamwise–wall normal plane, while contours of v_k remain vertical, and regions of peak positive u_k coincide roughly with regions of negative v_k. However, the wall-normal localization of the response modes depends on the mode speed c. For small c (small y_c^+), the streamwise and wall-normal velocities peak at an approximately constant wall-normal location that is above the critical layer for these slow-moving modes, $y^+ > y_c^+$. McKeon & Sharma (2010) consider such modes attached, since they have a significant near-wall velocity footprint. For large c, the velocities peak at the critical layer y_c^+, where the wave speed matches the local mean velocity. Such modes, which detach from the wall with increasing c, are considered critical by McKeon & Sharma (2010). For the wavenumber combination considered above, $(k, n) = (6, \pm 60)$ at $R^+ = 1100$, this transition from attachment to criticality occurs near $c \approx 0.5$ ($c^+ \approx 12$, figure 5). As such, the response mode with $c^+ \approx 11$ shown in figure 2 exhibits characteristics common to both classes, i.e. it may be considered both attached and critical.

Note that the resolvent analysis only predicts the shape ($\boldsymbol{u}_k$) and amplification (σ_k) of the velocity response modes at each wavenumber–frequency combination. It does not predict the relative amplitude and phase of each $\boldsymbol{u}_k$ present in the real flow. As is evident from (2.4)–(2.8), the amplitude and phase of each response mode $\boldsymbol{u}_k$ depend on the amplitude and phase of the forcing $\boldsymbol{f}_k$ present in the flow. Since this forcing comprises the nonlinear convective terms in the Navier–Stokes equations, $\boldsymbol{f}_k = (-\boldsymbol{u} \cdot \nabla \boldsymbol{u})_k$, the entire system of velocity response modes is interconnected (McKeon *et al.* 2013). The mean velocity profile $U(y)$ in the resolvent operator (2.4) is another point of connection in this system. Here, the discretized resolvent operator is constructed using mean velocity data from previous DNS (Wu & Moin 2008) and experimental studies (McKeon *et al.* 2004). However, in a more complete model, the mean velocity profile must be sustained by the Reynolds stress. So, the Reynolds

stress contributions from individual modes must sum to match the total Reynolds stress in the real flow.

2.3. *Rank*-1 *model for opposition control*

As shown schematically in figure 1, under opposition control the wall-normal velocity is measured at y_d, and blowing and suction are applied at the wall to oppose the measured velocity. The effects of this wall blowing and suction are included in the resolvent operator via the boundary condition for wall-normal velocity:

$$v_{\boldsymbol{k}}(0) + A_d v_{\boldsymbol{k}}(y_d) = 0. \tag{2.9}$$

For $A_d = 1$, $v_{\boldsymbol{k}}$ at the wall is equal and opposite to that at the detection plane, y_d, corresponding to opposition control (Choi *et al.* 1994). In general, A_d can be a complex coefficient. The phase of A_d determines the phase shift between the measured velocity and the wall-based blowing and suction, and the magnitude of A_d determines the relative strength of the sensed and actuated velocities. For example, $v_{\boldsymbol{k}}(0)$ is in phase with $v_{\boldsymbol{k}}(y_d)$ for $A_d = -1$, while $A_d = 0$ corresponds to no control and serves as the null case. Note that the detection plane locations quoted in the text throughout this paper are approximate. The discretized resolvent operators are constructed by applying the control boundary condition (2.9) at the closest grid point above these quoted values. The detection plane locations shown in the figures correspond to the true values.

The resolvent analysis proceeds as before, with the resolvent operator $\boldsymbol{\mathcal{H}}_{\boldsymbol{k}}$ (2.4) modified to account for boundary conditions corresponding to opposition control. Control has two potential effects within this framework. First, the structure of the velocity response $\boldsymbol{u}_{\boldsymbol{k}}$ can change relative to the null case, reflecting the boundary condition (2.9). Second, control can affect the singular values. If $\sigma_{\boldsymbol{k}}$ decreases due to the effects of control, the mode is suppressed. If $\sigma_{\boldsymbol{k}}$ increases, the mode is further amplified.

The drag change due to control can be estimated by considering the mean flow equation, i.e. (2.2) for $\boldsymbol{k} = (0, 0, 0)$, which can be expressed as

$$\Pi + \frac{1}{r}\frac{\partial}{\partial r}\left(-r\tau + \frac{r}{Re}\frac{\partial U}{\partial r}\right) = 0. \tag{2.10}$$

Here, τ is the Reynolds stress and $\Pi = -\partial P/\partial x$ is the mean pressure gradient. Subtracting the controlled case (subscript c) from the null case (subscript 0) yields

$$(\Pi_0 - \Pi_c) + \frac{1}{r}\frac{\partial}{\partial r}\left(-r\Delta\tau + \frac{r}{Re}\frac{\partial (U_0 - U_c)}{\partial r}\right) = 0, \tag{2.11}$$

where $\Delta\tau = \tau_0 - \tau_c$. From (2.11), it can be shown that the decrease in the pressure gradient required to maintain constant bulk-averaged velocity under control,

$$\int_0^1 (U_0 - U_c) r \,\mathrm{d}r = 0, \tag{2.12}$$

is given by

$$\Pi_0 - \Pi_c = 8\int_0^1 r^2 \Delta\tau \,\mathrm{d}r, \tag{2.13}$$

where the radial coordinate is normalized by pipe radius such that $r = 0$ represents the centreline and $r = 1$ represents the wall. Thus, the extent of any drag reduction is determined by the change in the mean Reynolds stress, and the weighting factor for the Reynolds stress is proportional to r^2 (Fukagata, Iwamoto & Kasagi 2002). Fukagata *et al.* (2002) showed that the total skin friction drag can be decomposed into a so-called laminar contribution and a contribution from the turbulent Reynolds stress. For constant bulk-averaged velocity, the laminar contribution, which is proportional to Re^{-1}, remains unchanged under control. So, any change in drag can be attributed to a change in Reynolds stress, as shown in (2.13). In normalized terms, this change in the turbulent contribution can be expressed as

$$DR = \frac{\displaystyle\int_0^1 r^2 \Delta\tau \, \mathrm{d}r}{\displaystyle\int_0^1 r^2 \tau_0 \, \mathrm{d}r}. \tag{2.14}$$

From here on, the term 'drag reduction' for our model will be used to denote the quantity shown in (2.14). Keep in mind that this only represents the reduction in the turbulent (Reynolds stress) contribution to drag. Since the laminar contribution remains unchanged under control, the normalized total drag reduction is lower than the normalized reduction in the turbulent contribution. For $Re = 5300$ ($R^+ = 180$), Fukagata *et al.* (2002) show that the laminar contribution amounts to 33 % of the total drag. Thus, the total drag reduction would be roughly two-thirds of the reduction in the turbulent contribution. However, the relative importance of the laminar contribution ($\propto Re^{-1}$) decreases with increasing Reynolds number. At $Re = 44\,000$ ($R^+ = 1100$), the laminar term contributes 7 % of the total drag, and so the total drag reduction is nearly identical to the reduction in the turbulent contribution.

The strength of the resolvent analysis is that it allows the effects of control to be considered on a mode-by-mode basis. Since the velocity response modes obtained from the resolvent analysis are Fourier harmonics, interaction between modes across different $\boldsymbol{k}$ does not contribute a mean (time-averaged) Reynolds stress. A mean Reynolds stress is only generated through the interaction between the streamwise and wall-normal velocity from the same mode. Assuming unit forcing for both the controlled and null cases, the velocity field for a given $\boldsymbol{k}$ is given by $\sigma_{k0}\boldsymbol{u}_{k0}$ for the null case and by $\sigma_{kc}\boldsymbol{u}_{kc}$ for the controlled case. With this unit forcing assumption, the change in the Reynolds stress contribution from mode $\boldsymbol{k}$ under control is given by

$$\Delta\tau_{\boldsymbol{k}} = \tau_{k0} - \tau_{kc} = -\tfrac{1}{2}\,\mathrm{Re}[(\sigma_{\boldsymbol{k}}^2 u_{\boldsymbol{k}}^* v_{\boldsymbol{k}})_0 - (\sigma_{\boldsymbol{k}}^2 u_{\boldsymbol{k}}^* v_{\boldsymbol{k}})_c]. \tag{2.15}$$

Here, Re( ) denotes the real component. From (2.15), it is clear that two different factors can contribute to a reduction in Reynolds stress (and therefore drag) under control: a reduction in amplification, such that $\sigma_{kc} < \sigma_{k0}$; and a change in the phase relationship between streamwise and wall-normal components of velocity, such that $-\mathrm{Re}(u_{\boldsymbol{k}}^* v_{\boldsymbol{k}})_c < -\mathrm{Re}(u_{\boldsymbol{k}}^* v_{\boldsymbol{k}})_0$.

Of course, (2.15) only estimates the change in the Reynolds stress contribution from a single mode. An estimate of the total change in Reynolds stress under control, $\Delta\tau$, requires knowledge of the relative amplitudes of all the different wavenumber combinations present in the real flow. As noted earlier, the gain analysis (2.6)–(2.8) does not yield this information, and so additional assumptions are required. In this paper, a simple estimate for the total change in Reynolds stress is obtained by

assuming unit forcing across all $\boldsymbol{k}$ combinations present in the flow, such that the uncontrolled velocity field is

$$\boldsymbol{u}_0 = \sum_n \int_{-\infty}^{\infty} \int_{-\infty}^{\infty} \sigma_{k0} \boldsymbol{u}_{k0} \, \mathrm{e}^{\mathrm{i}(kx+n\theta-\omega t)} \mathrm{d}k \, \mathrm{d}\omega, \tag{2.16}$$

and the controlled velocity field is

$$\boldsymbol{u}_c = \sum_n \int_{-\infty}^{\infty} \int_{-\infty}^{\infty} \sigma_{kc} \boldsymbol{u}_{kc} \, \mathrm{e}^{\mathrm{i}(kx+n\theta-\omega t)} \mathrm{d}k \, \mathrm{d}\omega. \tag{2.17}$$

Essentially, this broadband forcing ($\boldsymbol{f}_k = \boldsymbol{f}_{k,1}$ for all $\boldsymbol{k}$) assumption implies that the relative magnitudes of the velocity modes are set only by the relative magnitudes of the singular values, $\boldsymbol{u}_k = \sigma_{k,1}\boldsymbol{u}_{k,1}$ (see (2.6)–(2.8)), and so velocity responses with the highest σ_k dominate the flow field. With this assumption, the total change in Reynolds stress becomes

$$\Delta\tau = \tau_0 - \tau_c = \sum_n \int_{-\infty}^{\infty} \int_{-\infty}^{\infty} \Delta\tau_k \, \mathrm{d}k \, \mathrm{d}\omega, \tag{2.18}$$

where $\Delta\tau_k$ is the change in the Reynolds stress contribution from mode $\boldsymbol{k}$ (2.15).

Throughout this paper, the normalized drag change due to control is estimated using (2.14)–(2.18). Note that the use of (2.14) to estimate the total normalized drag change is not strictly accurate because of the aforementioned laminar contribution to drag, which remains constant under control (Fukagata *et al.* 2002). However, (2.15)–(2.18) are based on a rank-1 approximation, and assume unit forcing across all $\boldsymbol{k}$. With these assumptions, the Reynolds stress obtained by summing the contributions from individual modes does not match the true Reynolds stress profile. In other words, the relative magnitudes of the laminar and turbulent (i.e. Reynolds stress) contributions to drag are not consistent with that in the real flow. So, it makes more sense to estimate just the relative change in the turbulent contribution to drag. Further, these assumptions do not satisfy the requirement that the assumed mean velocity profile be sustained by the Reynolds stress through (2.10). In a more complete model, the Reynolds stress profile can be matched to the real flow by assigning different weights to individual modes and by considering higher-rank approximations.

This model also assumes that the mean velocity profile remains constant, given by previous DNS results (Wu & Moin 2008) or experimental measurements (McKeon *et al.* 2004). In reality, control alters the Reynolds stress profile, and so the mean velocity profile also changes. Since the resolvent operator is constructed using mean velocity data (2.4), this change in velocity profile could affect the amplification characteristics of the forcing–response system. The simple model developed here does not yet account for this change in mean flow. Despite these simplifying assumptions, the following sections show that the model captures many trends previously observed in DNS and LES studies of opposition control.

3. Results and discussion

3.1. *A single mode*

The coherent structures that characterize the dynamically important near-wall cycle are known to have streamwise length scale $\lambda_x^+ \approx 1000$, spanwise length scale $\lambda_\theta^+ \approx 100$ and characteristic propagation speed $c^+ \approx 10$ (Robinson 1991). As a result, this section considers the effect of control on the mode $\boldsymbol{k} = (6, \pm 60, 0.45)$ at $R^+ = 1100$ shown in § 2.2, which has velocity and length scales $\lambda_x^+ \approx 1200$, $\lambda_\theta^+ \approx 120$ and $c^+ \approx 11$.

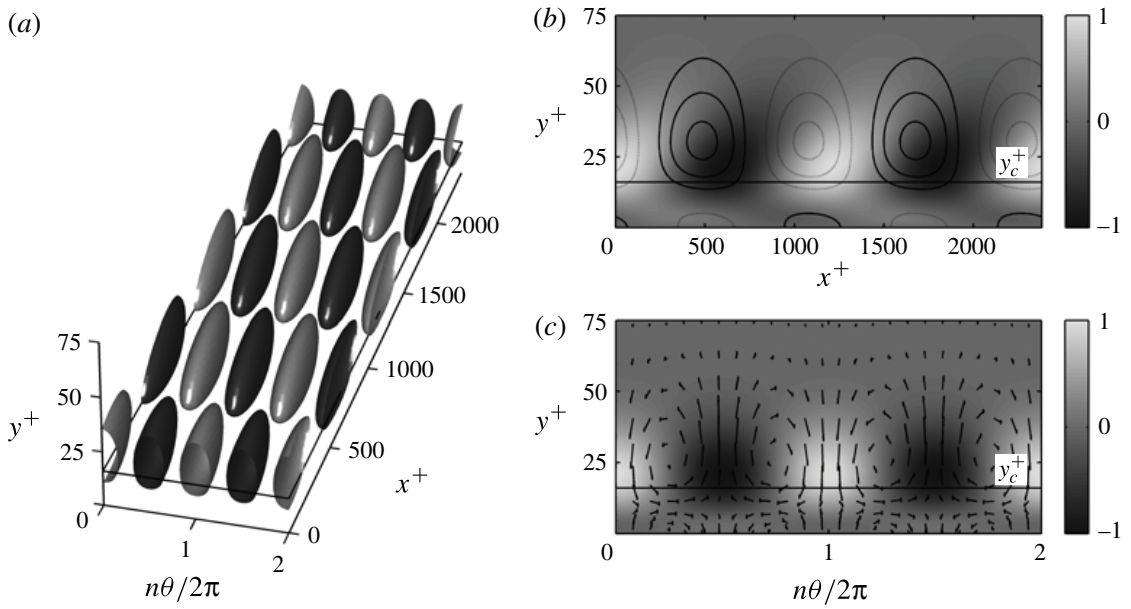

FIGURE 4. Velocity structure for the combination of modes $\boldsymbol{k} = (6, \pm 60, 0.45)$ under opposition control with the detection plane at $y_d^+ \approx 15$. For greater detail, see caption for figure 2.

The null case amplitude and phase profiles in figure 3 (solid lines) represent the velocity structure shown in figure 2. The magnitude of the streamwise velocity (black line) peaks near the critical layer, $y_c^+ = 16$, while the wall-normal velocity (grey line) peaks slightly further from the wall at $y^+ \approx 30$. The phase of $u_{\boldsymbol{k}}$ decreases with increasing y^+, while the phase of $v_{\boldsymbol{k}}$ remains roughly constant. In other words, isocontours of $u_{\boldsymbol{k}}$ lean downstream but isocontours of $v_{\boldsymbol{k}}$ remain vertical, as can be seen in figure 2(*b*). Further, the streamwise velocity is π out of phase with the wall-normal velocity near the critical layer, such that regions of positive $u_{\boldsymbol{k}}$ coincide with region of negative $v_{\boldsymbol{k}}$, and vice versa. Note that this phase relationship between $u_{\boldsymbol{k}}$ and $v_{\boldsymbol{k}}$ ensures that the Reynolds stress contribution from this mode also peaks near the critical location (figure 3*c*).

Figures 3 and 4 show how the velocity structure for this mode is affected by opposition control with the detector at $y_d^+ \approx 15$. Above the detection plane, the phase profiles for $u_{\boldsymbol{k}}$ and $v_{\boldsymbol{k}}$ do not show a significant change under control (figure 3*b*, dashed lines). The phase of $v_{\boldsymbol{k}}$ remains approximately constant with distance from the wall, while the phase of $u_{\boldsymbol{k}}$ decreases. However, the phase of $v_{\boldsymbol{k}}$ jumps by π between the detection plane and the wall, so that the $v_{\boldsymbol{k}}(y_d^+)$ and $v_{\boldsymbol{k}}(0)$ are of opposite sign. In addition, the magnitude of $v_{\boldsymbol{k}}$ exhibits a sharp dip at $y^+ \approx 10$, halfway between the detection plane and the pipe wall (figure 3*a*). Similar to previous DNS observations (Hammond *et al.* 1998; Chung & Talha 2011), this suggests that a virtual wall is established, which hinders the transfer of momentum (figure 4*b*,*c*). Further, opposition control displaces the location of peak $u_{\boldsymbol{k}}$ for this mode away from the critical layer to $y^+ \approx 22$ (figures 3*a* and 4*a*). This upward displacement indicates that opposition control may weaken the critical-layer mechanism responsible for high amplification.

Despite these structural changes, the normalized Reynolds stress contribution from this mode does not change considerably under control (figure 3*c*). The location of the peak Reynolds stress is displaced upwards relative to the null case, and an additional smaller peak in Reynolds stress can be seen close to the wall. Importantly, the

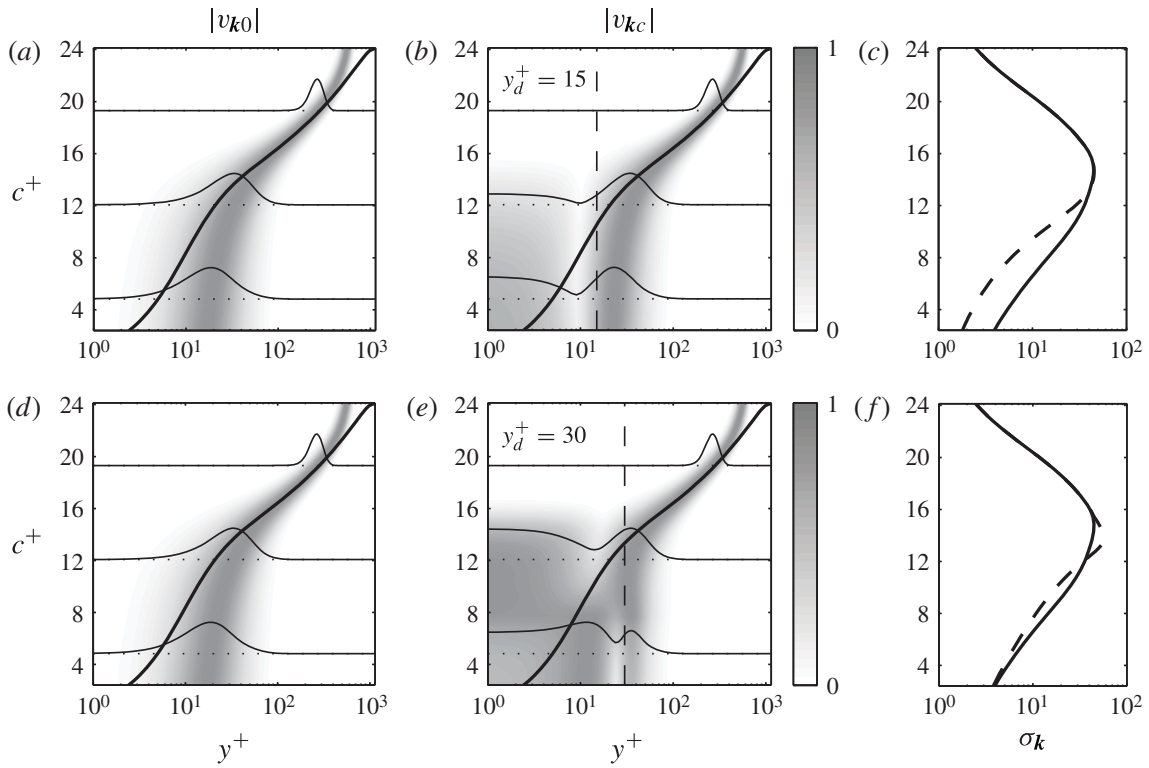

FIGURE 5. Effect of opposition control on the modes $\boldsymbol{k} = (6, 60, c)$, with phase speed ranging from $c = 0.1$ to 1.0 ($c^+ = 2.4$ to 24). The detection plane is located at $y_d^+ \approx 15$ in panels (*a–c*) and at $y_d^+ \approx 30$ in panels (*d–f*). (*a*,*d*) The normalized distribution of vertical velocity for the null case, $|v_{k0}|$. (*b*,*e*) The normalized velocity distribution for the controlled case, $|v_{kc}|$. The bold black lines show the critical-layer location, y_c^+. (*c*,*f*) Singular values for the null (solid line) and controlled cases (dashed line).

resolvent analysis predicts much lower gain for this mode under control, consistent with the establishment of a virtual wall and the weakening of the critical-layer mechanism. Specifically, the singular value for this mode drops from $\sigma_{k0} = 29.5$ to $\sigma_{kc} = 18.1$. Under the unit forcing assumption employed here, this decrease in amplification equates to a 39 % decrease in mode strength. Since the Reynolds stress depends on squared singular values (2.15), control reduces the drag contribution from this mode by nearly 60 % even though the normalized Reynolds stress contribution shown in figure 3(*c*) does not change significantly.

3.2. *Mode attachment and detection plane elevation*

To provide greater insight into the broader effects of opposition control, including the deterioration of control performance with sensor elevation, this section considers modes with the same spatial scales as the previous section ($k = 6$, $n = \pm 60$), but with varying speed $c^+ = 2.4$–24 ($0.1U_{CL}^+$–$1.0U_{CL}^+$) and sensor location y_d^+. Figure 5(*a*,*d*) shows that the radial footprint of the resolvent modes is determined by the mode speed c^+, which can be thought of as the convection speed for the velocity structure associated with the modes. For modes with $c^+ < 12$, the location of the peak wall-normal velocity remains roughly constant at $y^+ \approx 20$–30. These slower-moving modes have a significant near-wall velocity signature. Following McKeon & Sharma (2010)

and McKeon *et al.* (2013), such modes are considered attached to the wall. As the mode speed increases above $c^+ > 12$, the velocity footprint of the modes is lifted up from the wall, and the location of the peak wall-normal velocity tracks the critical layer, where the mode speed matches the mean velocity, $U^+(y_c^+) = c^+$. Such modes are termed critical; although, do bear in mind that this classification of modes is, to some degree, subjective. Modes of intermediate speed $c^+ \approx 10$–14 exhibit characteristics common to both classes of mode (i.e. localization around critical layer and near-wall velocity presence).

Opposition control with the detection plane at $y_d^+ \approx 15$ leads to the generation of significant near-wall blowing and suction for modes with speed $c^+ \leqslant 12$ (figure 5*b*). This actuation leads to the establishment of a virtual wall at $y^+ \approx 10$, where the magnitude of the wall-normal velocity is close to zero. The magnitude of the blowing and suction generated decreases as $c^+ > 12$, and little or no blowing and suction is generated at the wall for faster modes with $c^+ > 16$. Physically, this is because these faster-moving modes become localized around their respective critical layers at $y_c^+ > 20$, and so they do not have a strong velocity signature near $y^+ = 15$. The sensor at $y_d^+ \approx 15$ does not detect these modes, and so little blowing or suction is generated at the wall. However, as the detection plane moves further away from the wall to $y_d^+ \approx 30$, the sensor does pick up some of these faster-moving modes. Figure 5(*e*) shows that, for $y_d^+ \approx 30$, significant blowing and suction are generated for modes with speeds up $c^+ \leqslant 16$. Consistent with these observations, opposition control only affects the singular values for modes with speed $c^+ < 12$ with the sensor at $y_d^+ \approx 15$ (figure 5*c*), and for modes with speed $c^+ < 16$ with the sensor at $y_d^+ \approx 30$ (figure 5*f*). Faster-moving modes remain unaffected by control because little blowing and suction are generated at the wall to oppose their motion.

For both $y_d^+ \approx 15$ and $y_d^+ \approx 30$, opposition control suppresses modes with $c^+ \leqslant 12$. The singular values for these modes decrease under control, $\sigma_{\boldsymbol{k}c} < \sigma_{\boldsymbol{k}0}$ (figure 5*c*,*f*). As discussed earlier, a lower singular value leads to decreased mode strength and Reynolds stress, and so the drag contribution from these modes decreases under control. This decrease in amplification is probably associated with the establishment of the virtual wall near $y^+ \approx 10$ (figure 5*b*,*e*). However, with the sensor at $y_d^+ \approx 30$, modes with speed $c^+ \approx 12$–16 are further amplified due to control; the singular values for these modes increase $\sigma_{\boldsymbol{k}c} > \sigma_{\boldsymbol{k}0}$ (figure 5*f*). Since the transition from attached to critical modes occurs near speed $c^+ \approx 12$, these results suggest that attached modes are suppressed by opposition control, while critical modes may be further amplified.

Figures 6 and 7 show the effect of opposition control on the velocity structure for one such critical mode: $\boldsymbol{k} = (6, 60, 0.55)$, with $c^+ = 0.55U_{CL}^+ = 13.2$. The singular value for this mode increases from $\sigma_{\boldsymbol{k}0} = 43.0$ to $\sigma_{\boldsymbol{k}c} = 53.8$ under control. Unlike the mode $\boldsymbol{k} = (6, 60, 0.45)$ shown in figures 2–4, opposition control does not affect the location of the peak streamwise and wall-normal velocity in this case (figure 6*a*). The peak in streamwise velocity remains near the critical layer under control, suggesting that the critical-layer amplification mechanism remains largely unaffected. Further, even though a virtual wall is established ($y^+ \approx 15$, figure 6*a*), in this case the virtual wall is further from the critical layer (and hence the location of peak streamwise velocity) compared to the case shown earlier in figure 3(*a*). So, the virtual wall does not hinder momentum transfer from the mean flow to $u_{\boldsymbol{k}}$ via lift-up to the same extent. Thus, opposition control merely generates additional Reynolds stress (figure 6*c*) and vortical structure (figure 7*b*) close to the wall for these faster-moving critical modes. It does not fundamentally change the structure of these response modes such that their

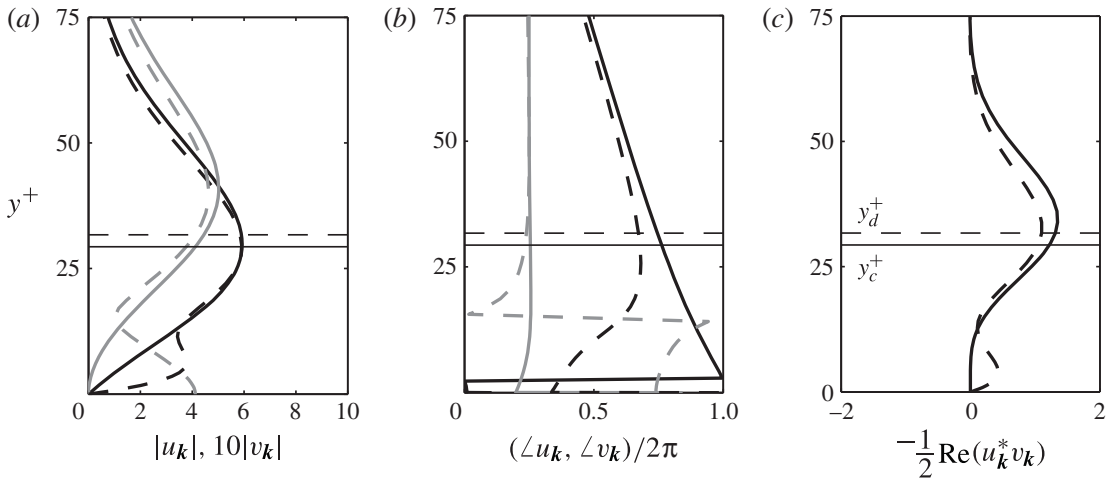

FIGURE 6. Vertical profiles showing (*a*) the amplitude and (*b*) the phase of the streamwise (black) and wall-normal (grey) velocity for mode $\boldsymbol{k} = (k, n, c) = (6, 60, 0.55)$ at $R^+ = 1100$ ($c^+ = 13.2$). (*c*) The Reynolds stress contribution from this mode. Solid lines show the null case, and dashed lines represent the controlled case. Horizontal lines show the critical layer ($y_c^+ = 29$) and detection plane ($y_d^+ = 31$). The singular values for the null and controlled cases are $\sigma_{k0} = 43.0$ and $\sigma_{kc} = 53.8$, respectively.

singular values decrease. Note that these observations are consistent with the DNS of Hammond *et al.* (1998), who showed that opposition control with the detection plane at $y_d^+ \approx 25$ enhances the vertical transfer of momentum close to the wall when a quasi-streamwise vortex appears above the detection plane.

3.3. *Effect of opposition control in spectral space*

The results presented in § 3.2 show that opposition control suppresses some modes but amplifies others, and so the overall effectiveness of control is likely to be determined by the relative strength of these suppressed and amplified modes. To provide further insight into this trade-off between modes, figure 8 shows model predictions for $R^+ = 180$ in spectral λ_x^+–c^+ space. Note that these data represent summations over the range of azimuthal wavenumbers $n = \pm(0\text{–}316)$. In general, there is close correspondence between the normalized change in drag (figure 8*a*,*c*) and the normalized change in squared singular values (figure 8*b*,*d*), suggesting that mode suppression (lower σ_k) is the primary drag reduction mechanism in the model developed here. This result is consistent with the singular value analysis of control pursued by Lim & Kim (2004), as well as the correlation between streak amplification and turbulent skin friction reduction observed by Duque-Daza *et al.* (2012).

Figure 8 also confirms the trends observed for individual modes in § 3.2. Modes with $c^+ > 14$ remain largely unaffected by control with the sensor at $y_d^+ \approx 10$. The critical layer for these faster modes is located at $y_c^+ > 30$, and so they do not have a strong velocity signature at the sensing plane $y_d^+ \approx 10$. Similarly, smaller slower-moving modes ($\lambda_x^+ \leqslant 10^2$, $c^+ < 12$) remain unaffected by opposition control with the sensor placed further away from the wall at $y_d^+ \approx 30$. The critical layers for these modes fall below $y_c^+ < 18$, indicating that they are energetic below the sensing plane. Note that, for $y_d^+ \approx 30$, longer modes with $\lambda_x^+ > 10^3$ are affected by opposition control regardless of their speed. In other words, modes with large streamwise wavelengths tend to have a longer-range effect on the sensor. This is because the wall-normal

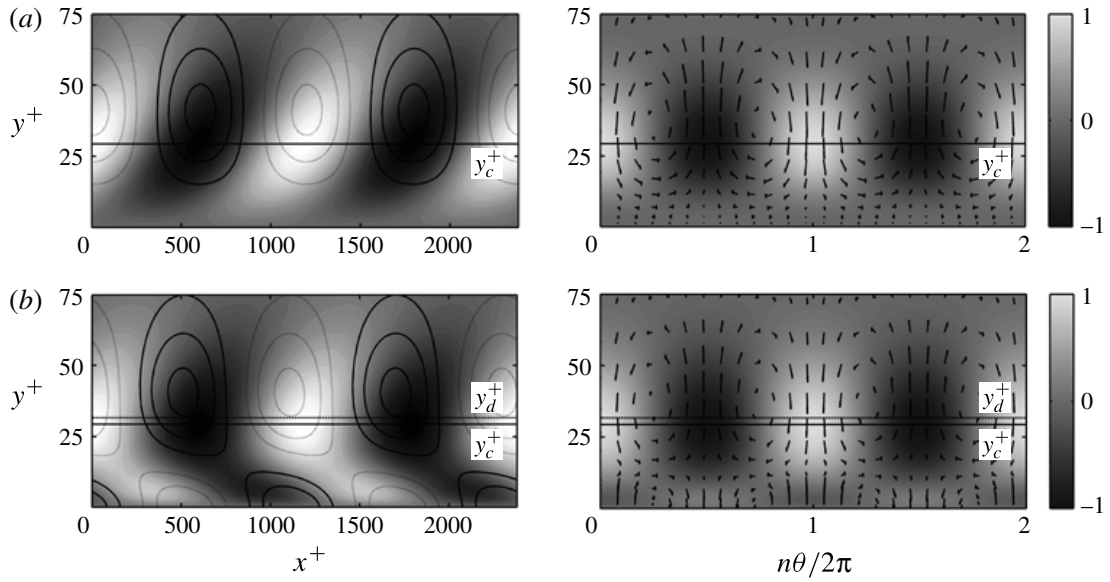

FIGURE 7. Velocity structure for the combination of modes $\boldsymbol{k} = (6, \pm 60, 0.55)$ at $R^+ = 1100$, for (*a*) the null case and (*b*) the controlled case, with $y_d^+ \approx 30$. The panels on the left show velocity isocontours in the streamwise–wall normal plane. The shading represents the streamwise velocity distribution. The solid and dashed lines represent positive and negative wall-normal velocity, respectively (at $\pm 0.3,\ 0.6,\ 0.9$ of maximum). The panels on the right show the velocity structure in the azimuthal–wall normal plane. The shading represents the streamwise velocity, while the arrows denote the wall-normal and azimuthal velocity fields.

extent of the resolvent modes increases with increasing wavelength, such that longer modes are also taller (McKeon & Sharma 2010).

A relatively straight line of the form $\log_{10}(\lambda_x^+) \sim c^+$ separates spectral regions that are positively and negatively affected by opposition control (dash-dotted lines in figure 8). Similar to the results shown in figure 5, slower modes tend to be suppressed by opposition control (e.g. $c^+ < 12$ for $\lambda_x^+ \approx 10^3$ in figure 8*c*,*d*) while faster modes tend to be amplified. Further, the wave speed at which this transition from drag reduction to drag enhancement occurs increases with increasing streamwise wavelength (e.g. $c^+ > 16$ for $\lambda_x^+ \approx 10^4$). The results presented in § 3.2 suggest that this change in behaviour could be attributed to a transition from attachment to criticality. Since longer modes have a larger wall-normal extent, they are likely to become critical at higher speeds (i.e. for higher y_c^+). This is confirmed by a comparison of the results shown in figures 5 and 9. For the $\boldsymbol{k} = (6, \pm 60, c)$ modes shown in figure 5, the wall-normal velocity peaked at $y^+ \approx 20$ at low wave speeds and the transition from mode suppression to mode enhancement occurred at $c^+ > 12$. For modes that are 10 times longer in the streamwise and spanwise directions, $\boldsymbol{k} = (0.6, \pm 6, c)$, the wall-normal velocity peaks further away from the wall at low wave speeds ($y^+ \approx 80$, figure 9*a*). These taller longer modes only localize around their respective critical layers for $c^+ > 16$, and this transition from attachment to criticality again coincides with a deterioration in control performance ($\sigma_{\boldsymbol{k}c} > \sigma_{\boldsymbol{k}0}$, figure 9*c*).

Under the broadband forcing assumption employed here, the model predicts that relatively short modes with $\lambda_x^+ \approx 10$–100 travelling at speeds $c^+ = 6$–14 are the most energetic at $R^+ = 180$, and that there is little energetic content at longer wavelengths $\lambda_x^+ > 10^3$ (dashed contour lines in figure 8). In real flows, modes associated with

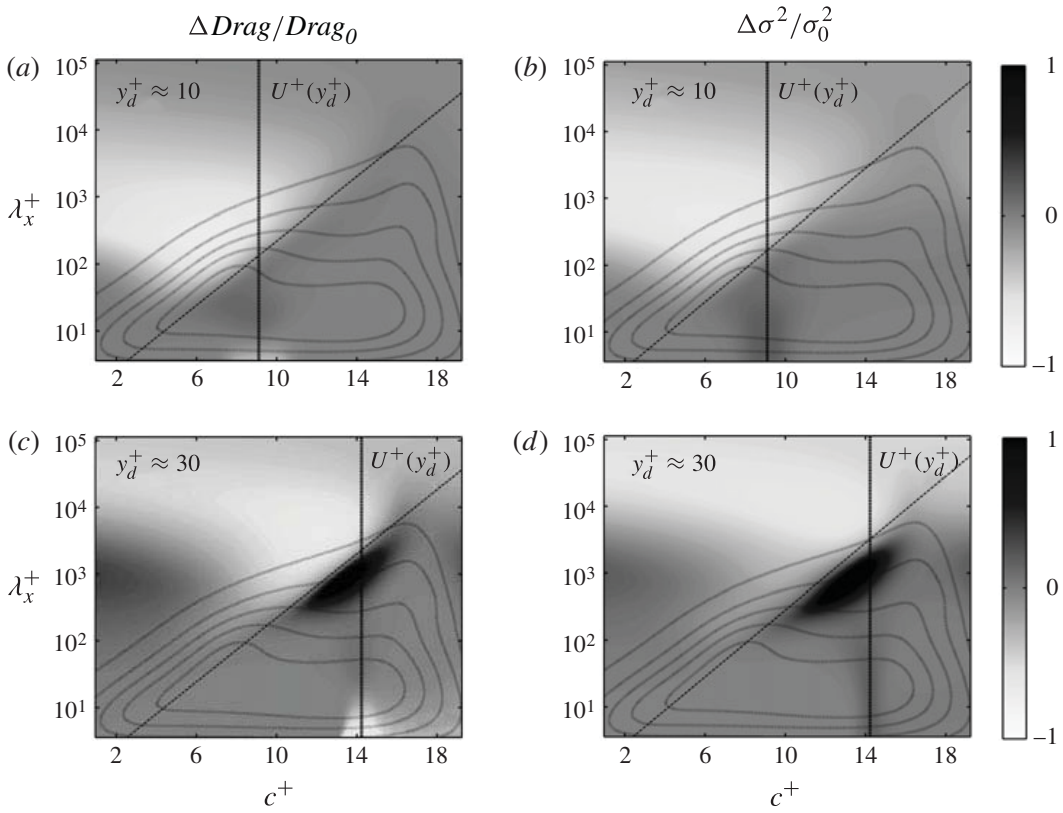

FIGURE 8. (*a*,*c*) Normalized change in the turbulent drag contribution (2.14) relative to the null case across the range of phase speed (c^+) and streamwise wavelength (λ_x^+) tested. Instead of the full expression shown in (2.18), these data represent shear stress summations over just the azimuthal wavenumber, n. (*b*,*d*) Normalized change in squared singular values relative to the null case. Light regions denote drag reduction (*a*,*c*) and mode suppression (*b*,*d*), while dark regions denote drag enhancement and mode amplification. The dashed contour lines show normalized, premultiplied singular values for the null case, $k^2\sigma_0^2$ (at values 0.1 (0.2) 0.9). The solid vertical lines represent the mean velocity at the detection plane. These results were obtained for Reynolds number $Re = 5300$ ($R^+ = 180$).

the near-wall cycle ($\lambda_x^+ \approx 10^3$, $c^+ \approx 10$–12) are known to be the most energetic at low Reynolds number (Monty *et al.* 2009; Smits *et al.* 2011). So, the energy content predicted by a broadband forcing assumption does not exactly match the energy content in real flows. Further, figure 8 shows much larger relative changes in drag in the spectral region corresponding to the near-wall cycle ($\lambda_x^+ \approx 10^3$, $c^+ \approx 10$) under control. The smaller slower-moving modes that are energetic under the broadband forcing assumption are not significantly affected by control. This discrepancy in energetic content between the model and real flows is likely to result in the model under-predicting total drag change.

Despite the discrepancy in energetic content, figure 8 provides significant physical insight into the deterioration of opposition control performance with increasing sensor elevation. A larger region of the spectral λ_x^+–c^+ space is negatively affected by control as the sensor is raised from $y_d^+ \approx 10$ (figure 8*a*,*b*) to $y_d^+ \approx 30$ (figure 8*c*,*d*). For $y_d^+ \approx 10$, few modes are detrimentally affected by opposition control. In contrast, for $y_d^+ \approx 30$, the drag contribution from modes with $\lambda_x^+ \approx 10^2$–10^4 and $c^+ \approx 10$–14 increases significantly. Physically, with the detection plane at $y_d^+ \approx 30$, the sensor is more likely to detect modes that are further amplified by opposition control.

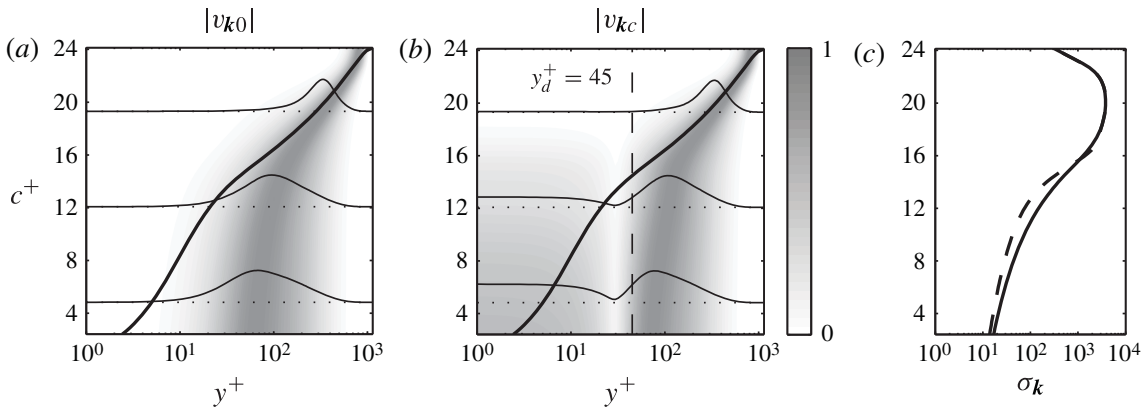

FIGURE 9. Effect of opposition control on the modes $\boldsymbol{k} = (0.6, 6, c)$, with phase speed ranging from $c = 0.1$ to 1.0 ($c^+ = 2.4$ to 24). The detection plane is located at $y_d^+ \approx 45$. (*a*) The distribution of vertical velocity for the null case, $|v_{k0}|$. (*b*) The velocity distribution for the controlled case, $|v_{kc}|$. (*c*) Singular values for the null (solid line) and controlled cases (dashed line). Bold black lines in panels (*a*,*b*) show the critical-layer location, y_c^+.

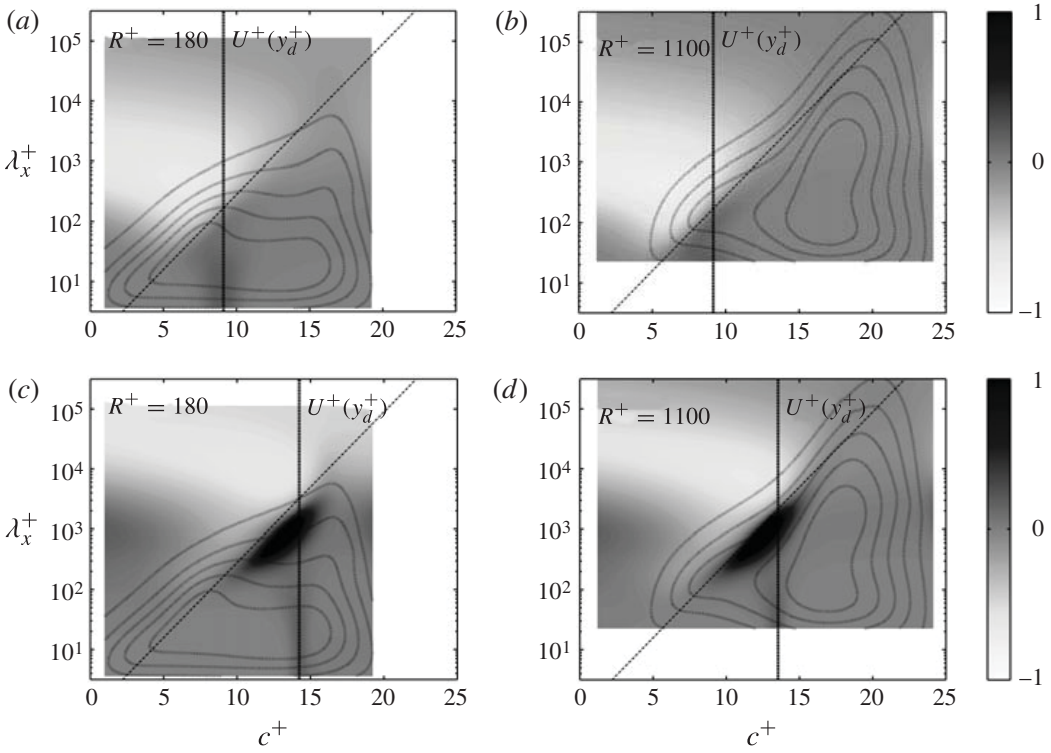

FIGURE 10. Normalized change in squared singular values relative to the null case for opposition control at (*a*,*c*) $R^+ = 180$ and (*b*,*d*) $R^+ = 1100$. The detection plane is set at $y_d^+ \approx 10$ for plots in panels (*a*,*b*) and at $y_d^+ \approx 30$ in panels (*c*,*d*). The dashed contour lines show normalized, premultiplied singular values for the null case, $k^2\sigma_{k0}^2$ (at values 0.1 (0.2) 0.9). The solid vertical lines represent the mean velocity at the detection plane.

Finally, the spectral maps shown in figure 10 may explain the deterioration in control performance with increasing Reynolds number. For roughly constant detection plane elevations, regions of drag reduction and drag enhancement are similarly

distributed for both $R^+ = 180$ (figure 10*a*,*c*) and $R^+ = 1100$ (figure 10*b*,*d*). Broadly, this suggests that the effect of opposition control on modes of the same wavelength λ_x^+ and wave speed c^+ is similar across Reynolds number. The key difference across Reynolds number is the initial energy content of such modes. Under the broadband forcing assumption, the model developed here predicts that a greater proportion of energy is concentrated in longer faster-moving modes at higher Reynolds number (dotted contour lines in figure 10). These faster modes are unaffected by opposition control when the detection plane is situated close to the wall at $y_d^+ \approx 10$ (figure 10*b*), and more likely to be detrimentally affected by opposition control when the detection plane is set at $y_d^+ \approx 30$ (see $\lambda_x^+ \approx 10^3$, $c^+ \approx 12$ in figure 10*d*). Hence, the drag reduction is diminished at higher Reynolds number. Of course, these results must be interpreted with some caution since the broadband forcing assumption employed here does not accurately capture the uncontrolled energy spectrum in the real flow. However, it is generally true that longer faster-moving modes become more energetic at higher Reynolds number (Smits *et al.* 2011).

3.4. *Drag reduction*

The rank-1 model developed in § 2.3 was used to estimate the drag reduction under opposition control at $Re = 5300$ ($R^+ = 180$) and $Re = 44\,000$ ($R^+ = 1100$). To arrive at these estimates, the Reynolds stress integrals in (2.18) were computed over the following wavenumber and wave speed ranges: $k = 0.01$–316, $n = \pm(0$–$316)$ and $c = 0.1$–1.0 (10–100 % of pipe centreline velocity). In inner units, these wavenumber and wave speed ranges correspond to $\lambda_x^+ \approx 4$–10^5, $c^+ \approx 1.9$–19 at $R^+ = 180$, and $\lambda_x^+ \approx 20$–7×10^5, $c^+ \approx 2.4$–24 at $R^+ = 1100$.

Figure 11(*a*) shows model predictions for drag reduction for a range of detection plane locations at $R^+ = 180$. The model predicts that maximum drag reduction is achieved with the sensor at $y_d^+ \approx 10$, and that drag increases for $y_d^+ > 25$. The maximum drag reduction predicted by the model (6 %) is much lower than that obtained in channel flow DNS (25 %) for similar Reynolds number, $Re_\tau = 180$ (Choi *et al.* 1994; Chung & Talha 2011). Further, the increase in drag past $y_d^+ > 25$ predicted by the model is less dramatic compared to the DNS results (figure 11*a*). However, the overall performance trend is captured reasonably well. At higher Reynolds number, $R^+ = 1100$, the maximum drag reduction decreases to 3 %.

Keep in mind that these model predictions represent only the reduction in the turbulent Reynolds stress contribution to drag (2.14). Since the so-called laminar contribution (33 % of the total drag at $R^+ = 180$, 7 % at $R^+ = 1100$) remains constant under control, the 6 % decrease in the Reynolds stress contribution at $R^+ = 180$ suggests a 4 % change in total drag, while the 3 % decrease at $R^+ = 1100$ suggests a 2.8 % decrease in total drag. This relative deterioration in opposition control performance with Reynolds number is also consistent with previous results. The channel flow LES of Pamies *et al.* (2007) suggests that the maximum drag reduction reduces from the 25 % observed in DNS at $Re_\tau = 180$ to 17.9 % at $Re_\tau = 960$. Despite the lack of quantitative agreement in total drag reduction, these results indicate that the resolvent analysis presents a powerful tool for understanding earlier phenomenological approaches to flow control and for predicting Reynolds-number trends.

Note that the results presented in this section were obtained using the simplest assumptions possible (rank-1 approximation, broadband forcing, no feedback to mean flow), and so the lack of quantitative agreement with previous DNS and LES results is

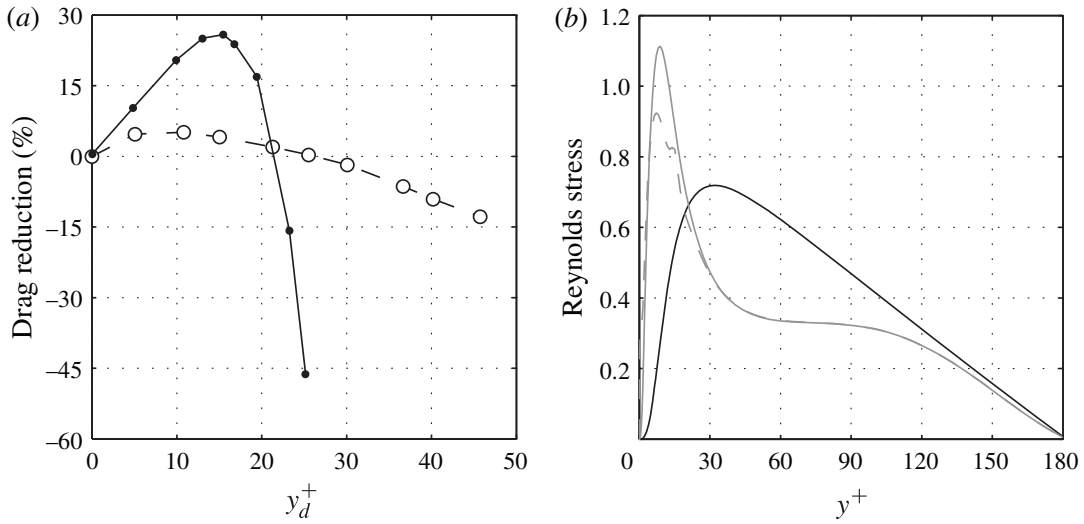

FIGURE 11. (*a*) Drag reduction plotted against detection plane location y_d^+. The open symbols represent predictions at $R^+ = 180$ using the rank-1 model developed here. The smaller closed symbols show channel flow DNS results from Chung & Talha (2011) at $Re_\tau = 180$. As noted earlier, the model results represent only the change in the turbulent Reynolds stress contribution to drag (2.14), while the DNS results represent the total drag reduction (i.e. including the laminar contribution; Fukagata *et al.* 2002). (*b*) Reynolds stress profiles from the DNS (black line) of Wu & Moin (2008), and those obtained here for the rank-1, broadband forcing model (grey lines). The solid grey line represents the null case, and the dashed line represents the controlled case with $y_d^+ \approx 15$. The modelled curves are normalized such that the area-weighted integral of the Reynolds stress for the uncontrolled case matches that from DNS.

to be expected. As noted in § 3.3, under the broadband forcing assumption, the model places greater emphasis on the smaller slower modes that are not significantly affected by control (figure 8). The drag change predicted by the model would be much larger if the resolvent modes are weighted to account for the greater energetic content of the near-wall cycle, bringing the predictions closer to DNS.

Further, the model assumptions do not satisfy the requirement that the mean profile be sustained through (2.10). In other words, the Reynolds stress profile obtained under the rank-1 and broadband forcing assumptions does not match that in the real flow. This is illustrated in figure 11(*b*), which compares the model Reynolds stress profile with that obtained in the pipe flow DNS of Wu & Moin (2008). The modelled profile (grey line) peaks closer to the wall ($y^+ \approx 10$, grey line) compared to the DNS profile ($y^+ \approx 30$, black line). Further, the model stress profile exhibits a brief plateau between $y^+ = 60$ and 90 rather than the near-linear decrease past $y^+ > 60$ observed in DNS. Since the Reynolds stress contribution from individual modes is expected to peak at or near the critical layer (figure 3*c*), the artificial near-wall peak in Reynolds stress may again be attributed to the greater emphasis placed on smaller slower modes with $c^+ < 10$ ($y_c^+ < 15$) in the model. More sophisticated assumptions (i.e. appropriate weighting of modes, higher-rank approximation) that correct the energetic inconsistency and make the mean profile self-sustaining are likely to improve quantitative agreement between model and DNS results.

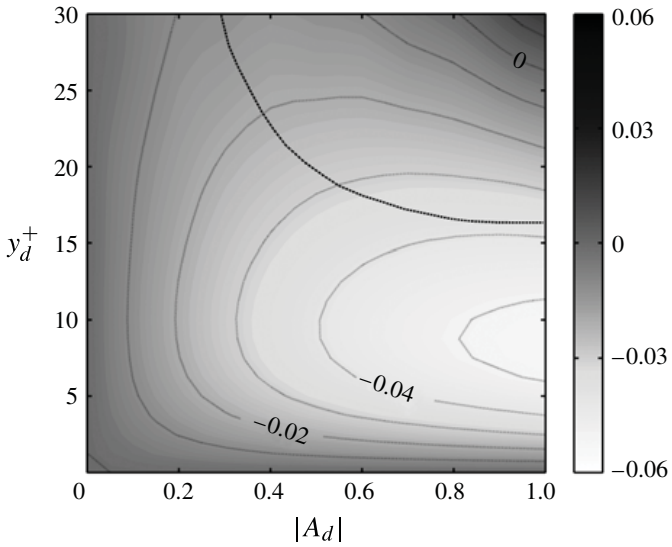

FIGURE 12. Contours showing drag change due to opposition control for varying detection plane elevation y_d^+ and actuation amplitude $|A_d|$, at $R^+ = 180$. The bold dashed line shows the optimal y_d^+–A_d relationship obtained in DNS by Chung & Talha (2011) at $Re_\tau = 180$.

3.5. *Amplitude and phase of wall blowing and suction*

Figure 12 shows model predictions for the drag reduction possible under opposition control executed with varying amplitude $|A_d|$ blowing and suction (2.9). In a recent DNS study, Chung & Talha (2011) showed that the deterioration in opposition control performance with increasing sensor elevation (figure 11*a*) can be offset by decreasing the amplitude of the blowing and suction generated at the wall. More specifically, Chung & Talha (2011) showed that the optimal amplitude decreases from $A_d = 1$ for $y_d^+ = 15$ to $A_d \approx 0.3$ for $y_d^+ = 30$, such that the velocity generated at the wall is 30 % of that at the sensor. The simple model developed here reproduces this trend reasonably well (figure 12). There are some quantitative differences: maximum drag reduction is achieved for $A_d = 1$ and $y_d^+ \approx 10$ in the model (cf. $y_d^+ \approx 15$ in DNS), and the optimal amplitude is $A_d \approx 0.4$ for $y_d^+ \approx 30$. However, these differences can again be attributed to the simple rank-1 and broadband forcing assumptions employed here.

Chung & Talha (2011) suggested that the improvement in performance with lower A_d comes about because the virtual wall created due to control is less effective at weakening the periodic downwash of high-momentum fluid when the amplitude of the wall blowing and suction is too large. The mode-by-mode deconstruction pursued here provides an alternative (albeit complementary) interpretation. The results presented in the previous sections show that the deterioration in control performance with increasing y_d^+ can be attributed to sensors far from the wall detecting modes that are further amplified by opposition control. So, a reduction in the amplitude of blowing and suction for increasing y_d^+ may constitute a damage limitation exercise, such that the positive effect of opposition control on attached modes is retained but the detrimental effect on critical modes is damped.

To illustrate this effect, figure 13 shows how varying-amplitude opposition control affects the set of modes considered in § 3.2: $\boldsymbol{k} = (6, \pm 60, c)$ at $R^+ = 1100$. Opposition control ($A_d = 1$) with the sensor at $y_d^+ \approx 30$ suppresses modes with $c^+ < 12$ and further amplifies modes with $c^+ = 12$–16 (figure 13*a*, solid line). Optimizing the amplitude

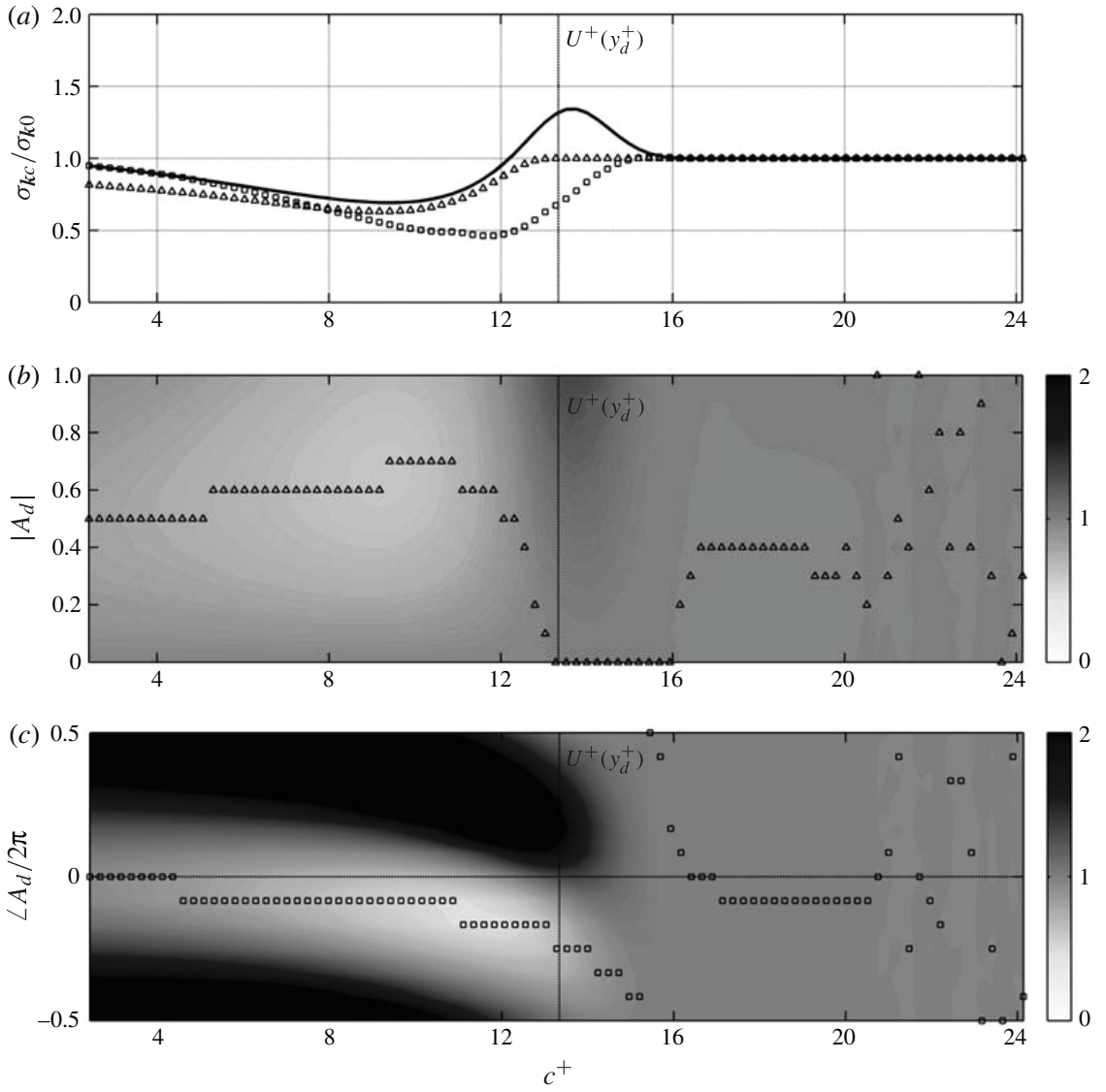

FIGURE 13. (*a*) Normalized singular values, $\sigma_{\boldsymbol{k}c}/\sigma_{\boldsymbol{k}0}$, for the modes $\boldsymbol{k} = (6,\ 60,\ c^+)$. The solid line shows results obtained for opposition control. Symbols correspond to control with optimized amplitude (triangles) and phase (squares). (*b*,*c*) Contours showing normalized singular values for opposition control with (*b*) varying amplitude $|A_d|$ and (*c*) varying phase $\angle A_d$. The markers denote the best case, corresponding to the symbols in panel (*a*). The detection plane is located at $y_d^+ \approx 30$.

of wall blowing and suction for each individual mode (i.e. for each c^+) leads to a modest improvement in performance. Modes with $c^+ < 12.5$ can be suppressed further (figure 13*a*, triangles) by employing blowing and suction amplitudes ranging from $A_d = 0.4$ to 0.7 (figure 13*b*). However, there is no remedy beyond switching off control entirely ($A_d = 0$) for modes with $c^+ \approx 13$–16. Note that faster modes with $c^+ > 16$ have a very weak velocity signature at the detection plane. The blowing and suction generated for such modes are near-zero regardless of $|A_d|$ and so they are not affected by any type of control with $y_d^+ = 30$ (figure 13*a*). Assuming that this limited set of modes is representative of the real flow, the trends shown in figure 13 explain the improvement in opposition control performance due to lower-amplitude blowing and

suction: attached modes are still suppressed (and perhaps more so) with a lower A_d, while critical modes experience more limited amplification.

Since A_d can be a complex coefficient (2.9), the model developed here can also be used to study the effect of a phase lag between measurement and actuation. Figure 13(*c*) explores the effect of this phase difference, $\angle A_d$, on control performance for the $\boldsymbol{k} = (6, \pm 60, c)$ modes. Here $\angle A_d = 0$ represents opposition control, i.e. $A_d = \exp(\mathrm{i}\angle A_d) = 1$. Positive $\angle A_d$ indicates that the wall blowing and suction lead the measured velocity (in time), while negative $\angle A_d$ indicates a phase lag. However, keep in mind that a $\pi/2$ phase lead is equivalent to a $3\pi/2$ phase lag under the Fourier decomposition employed here. Figure 13(*c*) (squares) shows that opposition control yields near-optimal results for attached modes with $c^+ < 10$; maximum mode suppression is achieved for phase $\angle A_d \approx 0$. However, the optimal $\angle A_d$ decreases with increasing wave speed. For $c^+ \approx 12$, greatest mode suppression is achieved when the velocity at the wall lags the velocity at the detection plane by $\approx \pi/3$. Control executed with this optimal phase lag results in close to 50 % mode suppression (figure 13*a*, squares), compared to ≈ 0 % for opposition control (figure 13*a*, full line). The optimal phase difference reduces further to $\angle A_d \approx -\pi$ for $c^+ \approx 16$, such that the velocity generated at the wall is in the same direction as that at the detection plane.

Importantly, figure 13(*a*) shows that critical modes that are further amplified by opposition control (e.g. $c^+ \approx 12$–16) may be suppressed with the introduction of a phase lag. Thus, a control law that is phase-optimized for individual modes could lead to significant performance improvements over opposition control. This optimization is explored briefly in the following section. At the same time, note that the optimal phase lag shown in figure 13(*c*) is normalized based on mode period, $T = 2\pi/\omega$, such that a $\pi/2$ phase lag denotes a temporal lag of $T/4$. Since modes of varying speed and wavelength also have varying period, the practical implementation of a phase-based control scheme, $\angle A_d$, is likely to be more challenging than the implementation of amplitude-based control, $|A_d|$.

3.6. *Optimization of control strategies*

This section briefly explores the development of optimal control strategies within the extended opposition control framework (known y_d^+, wall-based blowing and suction, complex A_d). To keep the analysis and discussion tractable, this optimization is only performed for the limited set of modes, $\boldsymbol{k} = (6, \pm 60, c)$ at $R^+ = 1100$, studied in §§ 3.2 and 3.5. The previous sections show that these modes exhibit a rich range of behaviour, which explains most previously observed trends for opposition control. This is further confirmed by the drag estimates shown in figure 14(*a*). Under traditional opposition control ($A_d = 1$), maximum drag reduction is achieved for $y_d^+ \approx 15$ and drag increases substantially for $y_d^+ > 30$ (figure 14*a*, circles). This is consistent with the DNS observations and full model predictions shown in figure 11. Control executed with an amplitude optimized for each detection plane results in a modest performance improvement, such that drag reduction (rather than enhancement) is achieved for $y_d^+ \leqslant 50$ (figure 14*a*, triangles). Further, the optimal amplitude decreases from $A_d = 1$ for $y_d^+ \leqslant 20$ to $A_d \approx 0.1$ for $y_d^+ \approx 50$ (figure 14*b*). These trends are also similar to those observed in previous DNS (Chung & Talha 2011). Note that these results were obtained by evaluating the integral in (2.18) only for $k = 6$, $n = \pm 60$, over $c = 0.1$–1.0 ($c^+ = 2.4$–24). Thus, an optimized control strategy could be developed for all modes; however, significant insight can be gained by considering control performance for a single (k, n) combination.

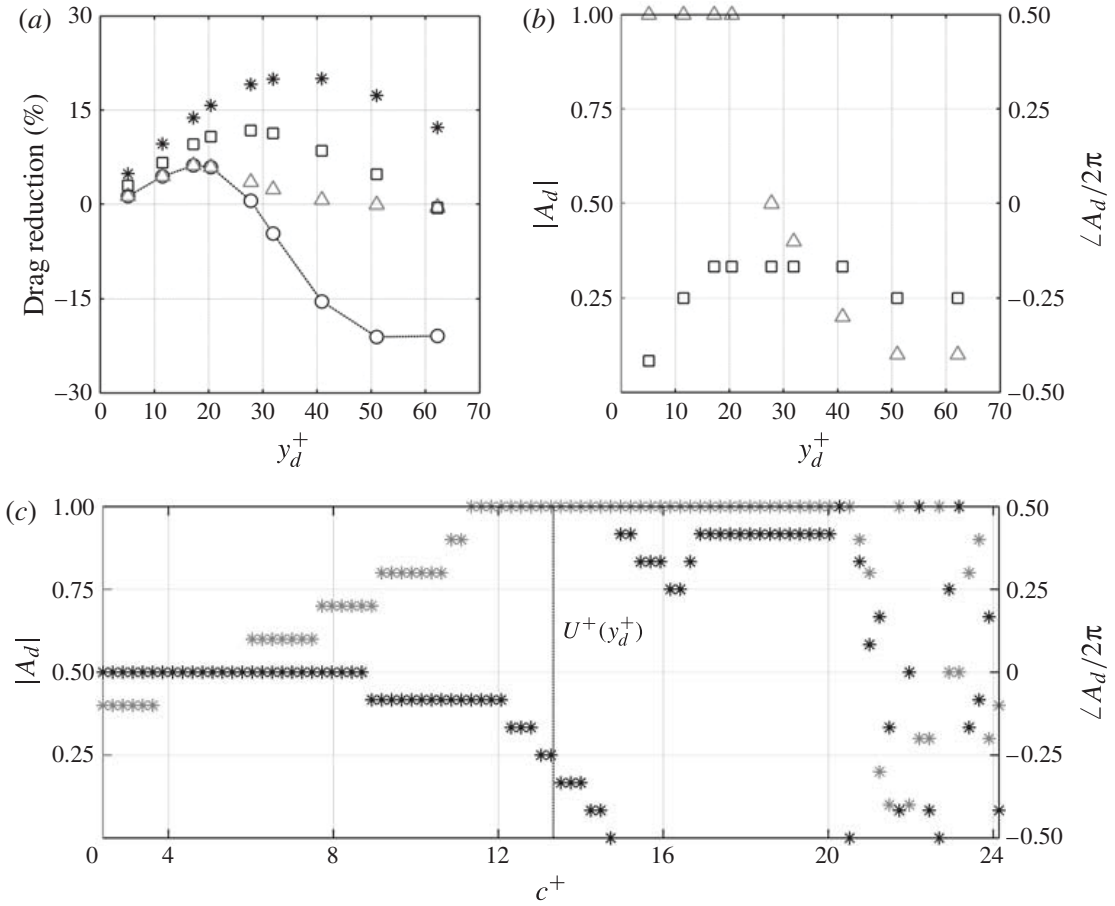

FIGURE 14. (*a*) Predicted drag reduction at varying detection plane locations y_d^+, summing together contributions from the modes $\boldsymbol{k} = (6, \pm 60,\ c = 0.1\text{–}1.0)$. The effects of traditional opposition control (circles), variable-phase control (squares), variable-amplitude control (triangles) and control optimized for individual modes (asterisks) are shown. (*b*) The optimal phase ($\angle A_d$, squares) and amplitude ($|A_d|$, triangles) at each detection plane elevation for the results shown in panel (*a*). (*c*) The phase (black asterisks) and amplitude (grey asterisks) of wall blowing and suction that leads to greatest reduction in singular value for each individual mode $\boldsymbol{k} = (6, \pm 60, c^+)$ with the detection plane at $y_d^+ \approx 30$.

Relative to traditional and varying-amplitude opposition control, control executed with a phase lag optimized for each detection plane yields a considerable improvement in performance. The maximum achievable drag reduction increases from 6 % to 14 % (figure 14*a*, squares). Further, figure 14(*b*) shows that the optimal phase difference is typically $\angle A_d = -\pi/3$ to $\angle A_d = -\pi/2$. Recall from figure 13(*c*) that these phase differences lead to critical modes, which are further amplified by opposition control, being suppressed. Since critical modes tend to be more energetic than attached modes under the broadband assumption employed here (higher $\sigma_{\boldsymbol{k}}$, figure 5*c*,*f*), they offer greater drag reduction potential. As a result, the phase optimization places greater emphasis on these critical modes compared to the attached modes, which require opposition control ($\angle A_d \approx 0$). Figure 15 shows that this improvement in performance with a phase lag between sensor and actuator velocity is also observed in the full model (i.e. integrating over all $\boldsymbol{k}$) at $R^+ = 180$. Specifically, the drag reduction increases from 6 % for opposition control with the sensor at $y_d^+ \approx 10$, to 8.5 % when a phase lag of $\angle A_d = -\pi/4$ is introduced. Further, figure 15 shows that the introduction

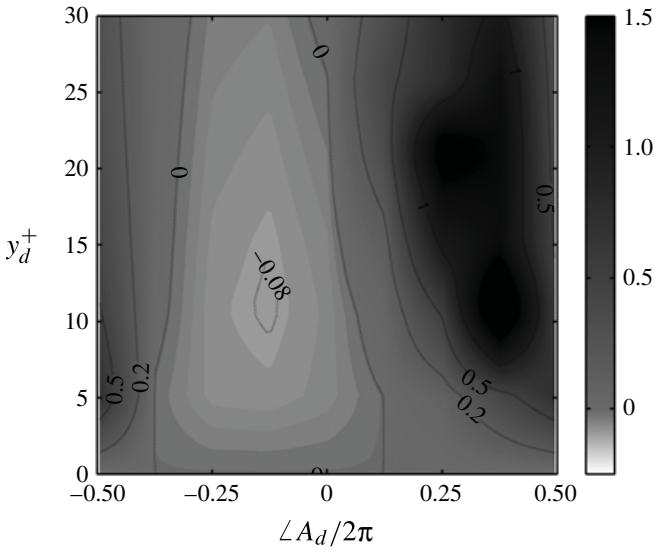

FIGURE 15. Contours showing normalized drag change due to control for varying detection plane elevation y_d^+ and phase-varying blowing and suction $\angle A_d$, at $R^+ = 180$. Note that $\angle A_d = 0$ represents opposition control.

of a phase lead $\angle A_d > 0$ results in a dramatic deterioration in performance, which is also consistent with the results shown in figure 13(*c*) for critical modes with speed $c^+ = 12$–16.

Figure 14(*a*) (black asterisks) shows that with blowing and suction optimized for each individual mode (i.e. each c^+), the maximum possible drag reduction increases to $\approx$20 % for $y_d^+ \approx 30$. This represents a three-fold improvement in performance over traditional opposition control. Moreover, significant drag reductions are obtained over the entire range of detection planes tested, $y_d^+ \approx 5$–60. The optimal phase $\angle A_d$ and amplitude $|A_d|$ for each mode is shown in figure 14(*c*). In general, these amplitudes and phases are consistent with the results shown in figure 13: slower modes ($c^+ < 8$) require low-amplitude opposition control ($\angle A_d = 0$ with $|A_d| < 1$), while critical modes with $c^+ \approx 12$–16 require a phase difference that decreases with increasing c^+ and high amplitudes ($A_d = 1$). Note that the detection plane location does not affect the optimal phases for the modes, but it does affect the optimal amplitudes (data not shown). This reflects the structure of the wall-normal velocity field for the response modes. The phase of $v_{\boldsymbol{k}}$ does not change in the wall-normal direction (see e.g. figure 3*b*), and so the optimal phase difference $\angle A_d$ between the sensor and the wall remains the same for different y_d^+. However, the amplitude of $v_{\boldsymbol{k}}$ does change in the wall-normal direction, and so the optimal amplitude ratio $|A_d|$ depends on the measurement location y_d^+.

4. Conclusion

With basic assumptions (rank-1, broadband forcing, no feedback to mean flow) and minimal computation, the model developed here is able to capture trends observed in previous DNS and LES studies of opposition control (§ 3.4). In general, each estimate for total drag reduction (i.e. for a fixed Reynolds number and detection plane) required less than a day of computation on one core of a laptop with 4 GB of RAM. No effort was made to make the computation efficient. Further, by considering the effects of

control on individual resolvent modes, the model provides new physical insight into the deterioration of control performance with increasing sensor elevation and Reynolds number. The results show that attached modes localized near the wall are suppressed by opposition control, while critical modes are further amplified (§ 3.2). Critical modes tend to be more energetic at higher Reynolds number, and they are more likely to be detected by sensors further from the wall. As such, the overall performance of opposition control depends on a trade-off between the magnitude and type of modes sensed (§ 3.3).

The analysis pursued here also suggests that critical modes, which are further amplified under traditional opposition control, may be suppressed with the introduction of a phase lag between sensor and actuator (§ 3.5). Preliminary results suggest that such mode-by-mode optimization of the control law could lead to significant overall performance improvement (§ 3.6). In this paper, the optimal amplitude and phase of wall blowing and suction for each mode were determined via a simple search across parameter space. However, the physical significance of these optimal phases and amplitudes of the wall blowing and suction remains to be understood. The forcing modes obtained under the resolvent analysis, $\boldsymbol{f_k}$ (2.6)–(2.8), may play a role. Intuitively, control is likely to be most effective when the wall-based actuation counteracts these high-gain forcing modes.

Although the model developed here is able to qualitatively reproduce previously observed DNS and LES trends, it significantly under-predicts the actual change in drag under opposition control (§ 3.4). This lack of quantitative agreement may be attributed to the rank-1 and broadband forcing assumptions. These assumptions imply that the turbulent flow field can be expressed purely as a superposition of the rank-1 response modes obtained under the resolvent analysis, and that the energetic content of each response mode is determined by the associated singular value. While rank-1 velocity responses are expected to contribute significantly to the flow field in real flows, higher-rank responses play a role too. Further, natural wall turbulence does not exhibit unit forcing across all wavenumber–frequency combinations (recall that the forcing represents gradients of the fluctuating Reynolds stresses). Therefore, to improve quantitative predictions, higher-rank modes must be included in the model and the variation in forcing strength with $\boldsymbol{k}$ must be accounted for via appropriate mode weighting. In practice, this would require estimating the energetic content of the first few resolvent modes present in natural flows at each wavenumber–frequency combination. Such estimates may be obtained via direct measurement or through matching spectra, Reynolds stress and turbulence intensity profiles obtained in DNS or experiment. One possible approach is detailed in Moarref *et al.* (2013), who develop a predictive model for the streamwise energy intensity in turbulent channel flow based on resolvent modes weighted as a function of the mode speed.

Note that including higher-rank modes does not affect the outcome of the phase and amplitude optimization pursued in § 3.6, which aims to reduce the first singular values (i.e. suppress the highest-gain velocity responses). While control affects all the modes present in the flow, any attempt to reduce the first singular values only requires consideration of the rank-1 forcing and response modes.

In its current form, the model also assumes that the mean velocity profile used to construct the discretized resolvent operator in (2.4) remains constant. Since control alters the mean Reynolds stress, the mean velocity profile also changes. This change in the mean velocity profile can affect the amplification characteristics of the resolvent operator (in a recent study, Brandt *et al.* (2011) showed that base flow modifications can affect noise amplification in laminar flat-plate boundary layers). The change

in amplification characteristics may, in turn, modify control performance. In future studies, this feedback via the mean flow could be incorporated into the model via an iterative procedure. In practical terms, this would involve starting with resolvent modes that are weighted in wavenumber–frequency space to capture the initial uncontrolled Reynolds stress profile in the flow, i.e. such that the mean velocity profile is self-sustaining in the model. The analysis can then proceed as described in this paper. In other words, the turbulent velocity fields and change in Reynolds stress contribution can be computed based on (2.16)–(2.18), albeit with the resolvent modes multiplied by the singular values as well as the wavenumber- and frequency-dependent weights. Next, the change in Reynolds stress can be used to estimate the controlled mean velocity profile. The resolvent analysis can then be repeated with this new profile to test how sensitive the results are to changes in the base flow.

Importantly, the resolvent analysis can contribute significantly to making turbulence flow control practicable. Since control performance is determined by what modes are being sensed, the analysis can help to guide sensor placement. Alternatively, for fixed sensor elevation, the analysis can help to define wavenumber–frequency bounds for control. Further, the wavenumber–frequency breakdown of control permitted by the resolvent analysis can help to alleviate any issues stemming from sensor and actuator resolution. In addition, one of the key technical challenges associated with the practical implementation of opposition control is that it requires off-wall velocity information (Koumoutsakos 1999). It has recently been shown that each resolvent mode has a distinct wall pressure signature that is $\pi/2$ out of phase with the wall-normal velocity field (Luhar *et al.* 2013). So, it may be possible to design effective flow control optimized for individual resolvent modes that requires only wall-based sensing.

Finally, the results presented here show that the resolvent analysis can be a powerful tool for the design and evaluation of control techniques. Although this paper focuses on opposition control, the approach presented herein can be extended to account for any linear control law. Control on spanwise velocity as suggested by Choi *et al.* (1994) or vorticity flux control as proposed by Koumoutsakos (1999) can be introduced via the boundary conditions on velocity and pressure, respectively. Similarly, the effect of compliant walls can be introduced into the resolvent framework via appropriate dynamic and kinematic boundary conditions; this is the subject of an ongoing research effort.

Acknowledgement

This material is based on work supported by the Air Force Office of Scientific Research under award FA9550-12-1-0469 (program manager Dr Douglas Smith).

REFERENCES

Bechert, D. W., Bruse, M., Hage, W., van der Hoeven, J. G. T. & Hoppe, G. 1997 Experiments on drag-reducing surfaces and their optimization with an adjustable geometry. *J. Fluid Mech.* **338**, 59–87.

Brandt, L., Sipp, D., Pralits, J. O. & Marquet, O. 2011 Effect of base-flow variation in noise amplifiers: the flat-plate boundary layer. *J. Fluid Mech.* **687**, 503–528.

Butler, K. M. & Farrell, B. F. 1993 Optimal perturbations and streak spacing in wall-bounded turbulent shear flow. *Phys. Fluids* **5** (3), 774–777.

Cattafesta, L. & Sheplak, M. 2011 Actuators for active flow control. *Annu. Rev. Fluid Mech.* **43**, 247–272.

CHOI, H., MOIN, P. & KIM, J. 1994 Active turbulence control for drag reduction in wall-bounded flows. *J. Fluid Mech.* **262**, 75–110.

CHOI, H., PARK, H., SAGONG, W. & LEE, S. 2012 Biomimetic flow control based on morphological features of living creatures. *Phys. Fluids* **24**, 121302.

CHUNG, Y. M. & TALHA, T. 2011 Effectiveness of active flow control for turbulent skin friction drag reduction. *Phys. Fluids* **23**, 025102.

DUQUE-DAZA, C. A., BAIG, M. F., LOCKERBY, D. A., CHERNYSHENKO, S. I. & DAVIES, C. 2012 Modelling turbulent skin-friction control using linearized Navier–Stokes equations. *J. Fluid Mech.* **702**, 403–414.

FUKAGATA, K., IWAMOTO, K. & KASAGI, N. 2002 Contribution of Reynolds stress distribution to the skin friction in wall-bounded flows. *Phys. Fluids* **14** (11), 73–76.

FUKAGATA, K. & KASAGI, N. 2002 Active control for drag reduction in turbulent pipe flow. In *Engineering Turbulence Modelling and Measurements* (ed. W. Rodi & N. Fueyo), vol. 5, pp. 607–616. Elsevier Science.

FUKAGATA, K., KERN, S., CHATELAIN, P., KOUMOUTSAKOS, P. & KASAGI, N. 2008 Evolutionary optimization of an anisotropic compliant surface for turbulent friction drag reduction. *J. Turbul.* **9** (35), 1–17.

GAD-EL HAK, M. 2000 *Flow Control: Passive, Active, and Reactive Flow Management*. Cambridge University Press.

HAMMOND, E. P., BEWLEY, T. R. & MOIN, P. 1998 Observed mechanisms for turbulence attenuation and enhancement in opposition controlled wall-bounded flows. *Phys. Fluids* **10** (9), 2421–2423.

HENNINGSON, D. S. & REDDY, S. C. 1994 On the role of linear mechanisms in transition to turbulence. *Phys. Fluids* **6** (3), 1396–1398.

HÖGBERG, M., BEWLEY, T. R. & HENNINGSON, D. S. 2003 Relaminarization of $Re_\tau = 100$ turbulence using gain scheduling and linear state-feedback control. *Phys. Fluids* **15**, 3572–3575.

JOSHI, S. S., SPEYER, J. L. & KIM, J. 1997 A systems theory approach to the feedback stabilization of infinitesimal and finite-amplitude disturbances in plane Poiseuille flow. *J. Fluid Mech.* **332**, 157–184.

KIM, J. 2011 Physics and control of wall turbulence for drag reduction. *Phil. Trans. R. Soc.* A **369**, 1396–1411.

KOUMOUTSAKOS, P. 1999 Vorticity flux control for a turbulent channel flow. *Phys. Fluids* **11**, 248–250.

LIM, J. & KIM, J. 2004 A singular value analysis of boundary layer control. *Phys. Fluids* **16**, 1980–1988.

LUHAR, M., SHARMA, A. S. & MCKEON, B. J. 2013 Wall pressure fluctuations induced by coherent structures in turbulent pipe flow. In *Eighth International Symposium on Turbulence and Shear Flow Phenomena (TSFP-8), Poitiers, France, 28–30 August*.

MCKEON, B. J., JACOBI, I. & SHARMA, A. S. 2013 Experimental manipulation of wall turbulence: a systems approach. *Phys. Fluids* **25**, 031301.

MCKEON, B. J., LI, J., JIANG, W., MORRISON, J. F. & SMITS, A. J. 2004 Further observations on the mean velocity distribution in fully developed pipe flow. *J. Fluid Mech.* **501**, 135–147.

MCKEON, B. J. & SHARMA, A. S. 2010 A critical-layer framework for turbulent pipe flow. *J. Fluid Mech.* **658**, 336–382.

MESEGUER, A. & TREFETHEN, L. N. 2003 Linearized pipe flow to Reynolds number 10^7. *J. Comput. Phys.* **186** (1), 178–197.

MIN, T., KANG, S. M., SPEYER, J. L. & KIM, J. 2006 Sustained sub-laminar drag in a fully-developed channel flow. *J. Fluid Mech.* **558**, 309–318.

MOARREF, R. & JOVANOVIC, M. 2012 Model-based design of transverse wall oscillations for turbulent drag reduction. *J. Fluid Mech.* **707**, 205–240.

MOARREF, R., SHARMA, A. S., TROPP, J. A. & MCKEON, B. J. 2013 Model-based scaling and prediction of the streamwise energy density in high-Reynolds-number turbulent channels. *J. Fluid Mech.* **734**, 275–316.

MONTY, J. P., HUTCHINS, N., NG, H. C. H., MARUSIC, I. & CHONG, M. S. 2009 A comparison of turbulent pipe, channel and boundary layer flows. *J. Fluid Mech.* **632**, 431–442.

PAMIES, M., GARNIER, E., MERLEN, A. & SAGAUT, P. 2007 Response of a spatially developing turbulent boundary layer to active control strategies in the framework of opposition control. *Phys. Fluids* **19**, 108102.

QUADRIO, M. & RICCO, P. 2004 Critical assessment of turbulent drag reduction through spanwise wall oscillations. *J. Fluid Mech.* **521**, 251–271.

QUADRIO, M., RICCO, P. & VIOTTI, C. 2009 Streamwise-traveling waves of spanwise wall velocity for turbulent drag reduction. *J. Fluid Mech.* **627**, 161–178.

ROBINSON, S. K. 1991 Coherent motions in the turbulent boundary-layer. *Annu. Rev. Fluid Mech.* **23**, 601–639.

SCHOPPA, W. & HUSSAIN, F. 2002 Coherent structure generation in near-wall turbulence. *J. Fluid Mech.* **453**, 57–108.

SHARMA, A. S. & MCKEON, B. J. 2013 On coherent structure in wall turbulence. *J. Fluid Mech.* **728**, 196–238.

SHARMA, A. S., MORRISON, J. F., MCKEON, B. J., LIMEBEER, D. J. N., KOBERG, W. H. & SHERWIN, S. J. 2011 Relaminarisation of $Re_\tau = 100$ channel flow with globally stabilizing linear feedback control. *Phys. Fluids* **23**, 125105.

SMITS, A. J., MONTY, J., HULTMARK, M., BAILEY, S. C. C., HUTCHINS, N. & MARUSIC, I. 2011 Spatial resolution correction for wall-bounded turbulence measurements. *J. Fluid Mech.* **676**, 41–53.

TREFETHEN, L. N., TREFETHEN, A. E., REDDY, S. C. & DRISCOLL, T. A. 1993 Hydrodynamic stability without eigenvalues. *Science* **261** (5121), 578–584.

WU, X. & MOIN, P. 2008 A direct numerical simulation study on the mean velocity characteristics in turbulent pipe flow. *J. Fluid Mech.* **608**, 81–112.

XU, S., REMPFER, D. & LUMLEY, J. 2003 Turbulence over a compliant surface: numerical simulation and analysis. *J. Fluid Mech.* **478**, 11–34.